Modeling and experimental validation of thin, tightly rolled dielectric elastomer actuators

Article *in* Smart Materials and Structures · November 2021

DOI: 10.1088/1361-665X/ac34be

6 authors, including:

Johannes Prechtl
Universität des Saarlandes
10 PUBLICATIONS **40** CITATIONS
SEE PROFILE

Julian Kunze
Universität des Saarlandes
13 PUBLICATIONS **78** CITATIONS
SEE PROFILE

Giacomo Moretti
Universität des Saarlandes
62 PUBLICATIONS **639** CITATIONS
SEE PROFILE

Daniel Bruch
Universität des Saarlandes
11 PUBLICATIONS **76** CITATIONS
SEE PROFILE

Modeling and Experimental Validation of Thin, Tightly Rolled Dielectric Elastomer Actuators

J. Prechtl, J. Kunze, G. Moretti, D. Bruch, S. Seelecke and G. Rizzello

Department of Systems Engineering, Department of Materials Science and Engineering, Saarland University, Saarbrücken, Germany

E-mail: johannes.prechtl@imsl.uni-saarland.de

June 14th, 2021

Abstract.

Due to their large deformation, high energy density, and high compliance, dielectric elastomer actuators (DEAs) have found a number of applications in several areas of mechatronics and robotics. Among the many types of DEAs proposed in the literature, rolled DEAs (RDEAs) represent one of the most popular configurations. RDEAs can be effectively used as compact muscle-like actuators for soft robots, since they allow eliminating the need for external motors or compressors while providing at the same time a flexible and lightweight structure with self-sensing capabilities. To effectively design and control complex RDEA-driven systems and robots, accurate and numerically efficient mathematical models need to be developed. In this work, we propose a novel lumped-parameter model for silicone-based, thin and tightly rolled DEAs. The model is grounded on a free-energy approach, and permits to describe the electro-mechanically coupled response of the transducer with a set of nonlinear ordinary differential equations. After deriving the constitutive relationships, the model is validated by means of an extensive experimental campaign, conducted on three RDEA specimens having different geometries. It is shown how the developed model permits to accurately predict the effects of several parameters (external load, applied voltage, actuator geometry) on the RDEA electro-mechanical response, while maintaining an overall simple mathematical structure.

Keywords: Dielectric Elastomers (DE), Dielectric Elastomer Actuators (DEA), Rolled DEA, Core-Free, Modeling, Lumped-Parameter Model, Free-Energy

Submitted to: *Smart Mater. Struct.*

1. Introduction

The increasing need for soft and lightweight actuators, which can be used in application areas such as soft robotics and wearables, has generated a growing interest in Dielectric

Elastomer (DE) transducers. DEs represent a class of smart materials capable of large deformation, high compliance, high energy density and efficiency, lightweight, and self-sensing capabilities. A DE basically consists of a dielectric membrane (e.g., acrylic, rubber, or silicone) covered by compliant electrodes, forming a flexible capacitor. DE transducers can be used as actuators that convert an applied voltage into motion, as capacitive sensors of pressure/deformation, or eventually as generators that transform mechanical work into electrical energy [1]. Due to their high flexibility and ease of manufacturing, DE devices can be easily integrated into flexible structures such as soft robots [2, 3] and wearables [4, 5].

The operating principle of a DE actuator (DEA) is based on the so-called Maxwell stress. When a sufficiently high voltage is applied to the DE electrodes, attractive electrostatic forces are generated between the electrodes. As a result of this effect, the compliant dielectric in between is squeezed, thus undergoing a reduction in thickness and a subsequent expansion in area (due to the material incompressibility). This principle has been exploited to develop a large number of DEA configurations, such as stack actuators [6], strip-in-plane actuators [7], cone-shaped out-of-plane actuators [8], diamond-shaped actuators [9], as well as minimum energy structures [10], diaphragms [11], bowties [12], spiders [13], and rolls [14], to mention few examples.

Among the many proposed types of DEA configurations, rolled DEAs (RDEAs) represent one of the most popular ones. A RDEA can be obtained by tightly winding an initially flat DE membrane in a spiral- or cylinder-like shape. A RDEA appears as a suitable design solution for applications in which one is interested in minimizing space requirements and increasing at the same time the work output. Several types of RDEA configurations have been proposed in the literature, which mainly differ in terms of the adopted DE material (e.g., silicone [15, 16], acrylic [17, 18]), type of core (e.g., elastic [19, 20], hollow [21, 22], core-free [23, 14]), and actuation mode (e.g., push [24], pull [25], bending [26]).

Due to their specific geometric characteristics, RDEAs can be naturally used to replace actuation mechanisms commonly used in artificial muscles and soft robots, like pneumatic or tendon-driven ones [27]. Other than exhibiting a form factor similar to the one of those types of actuators, RDEAs offer additional advantages in terms of a simpler mechanical structure (since mechanical transmissions, motors, and compressors are no longer required) as well as self-sensing capabilities (i.e., they can work as actuators and sensors at the same time) [28].

In order to optimize the design of complex RDEA-driven systems and soft robots, as well as to develop real-time control and self-sensing algorithms, mathematical models need to be developed. It is well known that modeling of DE transducers is challenging, as it requires to account for several complex effects such as large deformations, electro-mechanical coupling, and kinematic nonlinearities. For the specific case of RDEAs, the rolling process introduces additional kinematic effects and inhomogeneities in the structure, which further complicate the modeling process. In the last few years, a number of authors have investigated modeling and simulation of RDEA transducers.

Several authors proposed models for describing RDEAs containing an elastic core. In [17], an acrylic RDEA with a spring core is investigated. A set of geometrical simplifications (fixed inner diameter, layers volume conservation) allowed the authors to find an algebraic relation for the distribution of radial strain inside the roll. The authors, however, did not develop an explicit mechanical model for the actuator. An analytical model for an acrylic RDEA with elastic core is discussed in [29]. In this paper, the authors focused on modeling and characterizing the blocking force behavior only. In [18], an axial-symmetric finite element model for an acrylic RDEA with an elastic core is presented. The developed model permits to predict the actuator displacement in response to an applied electro-mechanical load. Nonetheless, such a finite element formalism is unsuitable for real-time simulations and control application. In [30], the authors analyze the behavior of a bending-type acrylic RDEA with an elastic core. Also in this case, a finite element framework is adopted to describe the complex core motion. A further example of bending RDEA based on an acrylic elastomer is analyzed in [26]. In the paper, mathematical equations are derived to correlate the bending angle and lateral force of multiple-degree-of-freedom RDEAs with segmented electrodes. Modeling and simulation of core-free RDEA configurations has also received some attention in literature. Carpi and De Rossi presented in [31] an electro-mechanical model for a silicone-based DEA, shaped as a single-layer hollow cylinder. Their model permits to accurately predict the low-strain behavior of the transducer. In [32], Jones and Sarban presented a model for a coreless silicone-based RDEA. The actuator is described by means of a grey-box model, by assuming a second order stress-strain dynamics whose parameters are identified experimentally. In [25], the authors developed a finite element model for a core-free RDEA. The work aimed at evaluating the effects due to electrode-free roll area, and using them as a reference to develop a simplified analytical model. Nonlinear effects due to large deformation were neglected.

From the above discussion, it can be noted that the currently available approaches for RDEA modeling lack a general and uniform methodology, and are rather focused on the specific issues of the system under investigation. This is possibly due to the wide spectrum of RDEA configurations which have been investigated in the literature, which may differ in terms of material (acrylic, silicone), rolling geometry (cylinder, spiral), and core (elastic, hollow). Clearly, for many types of RDEA configurations, the development of accurate mathematical models capable of accounting for their specific features still represent an open problem. In addition to that, the development of model-based control and self-sensing strategies for RDEAs is still a largely unexplored research area, especially in the context of soft robotics applications.

In this paper, we propose a control-oriented lumped-parameter model for a specific class of RDEAs, consisting of silicone-based DE membranes tightly rolled in a thin and core-free structure. Such a novel RDEA design has been recently proposed in [14] as a means to increase the energy density of the transducer, while keeping the manufacturing process simple and repeatible. Since those types of RDEAs are intended to be used as artificial muscles in DE-driven soft robots, the development of accurate control-

oriented models turns out to be of fundamental importance. The model must allow describing large deformations and electro-mechanical coupling, as well as dissipative effects, in a lumped-parameter fashion. Moreover, since we intend to use the model for design optimization as well, we are also interested in describing how the RDEA electro-mechanical behavior scales with geometry. Once such type of RDEA model is made available, it can be eventually coupled with a model of an external system (e.g., a pre-stretching mechanism, a soft robotic structure) in a physically consistent way, and used to simulate the actuation performance of complex DEA systems. Starting from a general free-energy framework, we develop an accurate mathematical model which is capable to account for all the desired effects in a physics-based fashion. After developing a general model, suitable approximations are developed with the goal of reducing the computational complexity without significantly affecting the accuracy. Subsequently, experimental validation of the developed model is performed by means of a number of custom-developed RDEA specimens, characterized by different geometries. It is shown how the developed model permits to accurately reproduce the experimental data, in terms of force-displacement, blocking force, and capacitance behavior, in each one of the investigated scenarios. We remark that the present paper is an extension of our previous work in [33], in which preliminary results on RDEA modeling were presented. In particular, [33] proposes a model for RDEAs which is essentially based on available models for strip-shaped DE membranes. Such a first model is validated by means of tensile experiments conducted on a single specimen only. In this work, we substantially extend the results in [33] by proposing: a more general and physically consistent modeling framework for RDEAs; a systematic way to consistently approximate the general roll model without significantly affecting its accuracy; a more extensive experimental campaign which also includes blocking force and capacitance measurements; a validation of the model for several rolls with different geometries.

The remainder of this paper is organized as follows. The operating principle of the thin and core-free RDEA is briefly summarized in Section 2. Model development is discussed in Section 3, while experimental validation is presented in Section 4. Finally, concluding remarks and future research directions are outlined in Section 5.

2. System Description

In this paper we focus on a specific class of actuators, consisting of thin, core-free, silicone-based RDEAs. A detailed description of the operating principle and manufacturing process of such types of RDEAs has been previously published in [14]. In this section, we present a brief summary of the main results of [14], instrumental to the subsequent modeling study.

The considered type of RDEAs are manufactured starting from a stack of two silicone membranes (Wacker Elastosil 2030, 50 μm thick [34]), as shown in Figure 1a. Prior to stacking, a carbon-based electrode layer is screen-printed on the bottom side of each silicone membrane (depicted in red and black in Figure 1a). During manufacturing,

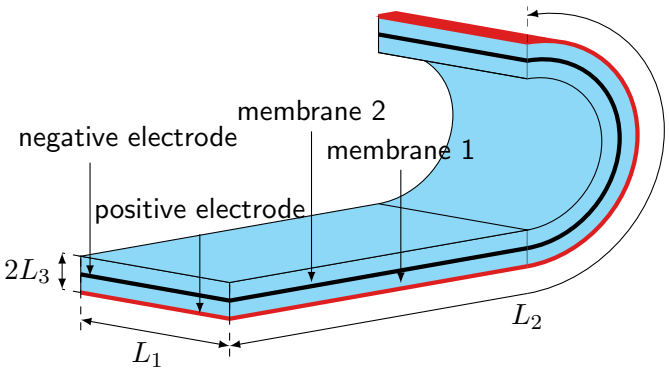

(a) Layers of the DE membrane before rolling.

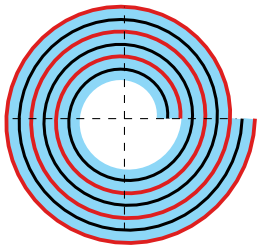

(b) RDEA layers after rolling, cross-sectional view.

(c) Picture of the resulting RDEA.

Figure 1: Design of the RDEA.

this stack is first prestretched by means of a support structure, then tightly rolled up, and crimped at both ends to integrate electrical and mechanical connections. For more details on manufacturing, the reader may refer to [14]. Due to the rolling process, the electrodes are distributed within the volume of the roll according to a spiral pattern, as shown in the cross-sectional sketch reported in Figure 1b. The end result consists of a core-free, thin, and wrinkle-free actuator structure. A picture of the resulting RDEA specimen is reported in Figure 1c.

When a high voltage is applied to the electrodes, an electric field is induced along the roll radial direction. The resulting Coulomb forces produce a compressive mechanical stress along the radial direction, called Maxwell stress, which causes the electrodes to attract each other [1]. These compressive forces cause the roll to reduce in radius and, as a result of the DE incompressibility, expand in length along the axis. This way, a thin artificial muscle actuator is obtained, capable to respond to an applied voltage with an increase of its length. The lack of a hollow core makes these type of actuators particularly compact, and attractive for applications where high-density linear actuation is required, such as soft robotic tentacle arms [35].

As a final remark, we point out that the RDEA must be axially pre-loaded in order to generate a stroke. The pre-load can be supplied, e.g., through a biasing mechanism, e.g., a mass, a spring, or a nonlinear mechanism [14, 35]. The choice of the biasing element turns out to be highly critical for the performance of the overall actuator system. Nevertheless, since the focus of the manuscript is on the RDEA unit itself, aspects related to the mechanical bias will not be considered hereafter.

3. Modeling

In this section, a lumped-parameter model for RDEAs is developed. Starting from a general free-energy framework, a detailed quasi-static model capable of describing the RDEA electro-mechanical response is first developed, and used as a reference. Subsequently, suitable approximations of this model are derived, which are capable of capturing the main features of the RDEA response in a more simple and computationally efficient way. Comparative studies are then conducted in simulation, in order to understand the operating ranges in which the developed approximations are capable of tightly approximating the reference model. Finally, a possible approach to incorporate rate-dependent viscoelastic effects within the developed quasi-static RDEA models is briefly discussed.

3.1. RDEA Lumped-Parameter Model 1: Three-Ring (3R)

The goal of this section is the development of a general quasi-static model for the actuator shown in Figure 2, accounting for different stress distributions for the material regions where electrodes are or are not present. When no load is applied to the roll, its undeformed length along the main axis equals L_1. If an electro-mechanical load consisting of an axial force F and a voltage v is applied to the roll, its axial length changes to l_1 (cf. Figure 2b).

It shall be noted that the roll is subject to complex deformation patterns and inhomogeneities, which are normally absent in conventional strip-shaped DEA membranes [36]. A relevant example is represented by the electric field within the rolled membrane, which possesses an inhomogeneous distribution along the cross-section due to the spiral-shaped geometry as well as due to the presence of electrode-free regions, see Figure 3a. To simplify the mathematical treatment, we introduce the following assumptions:

Assumption 1. The roll is always under tension, i.e., $F \geq 0$ and $l_1 \geq L_1$.

Assumption 2. Because of the friction among the elastomeric layers, when the roll is axially stretched, no slipping occurs between the adjacent DE layers.

Assumption 3. Edge effects due to the clamps and electrode-free edges are assumed negligible, and thus the strain is considered as uniform along the RDEA axis.

Assumption 4. Geometrical asymmetries due to the spiral shape are assumed as negligible. As a result, the geometry of the RDEA cross-section can be well

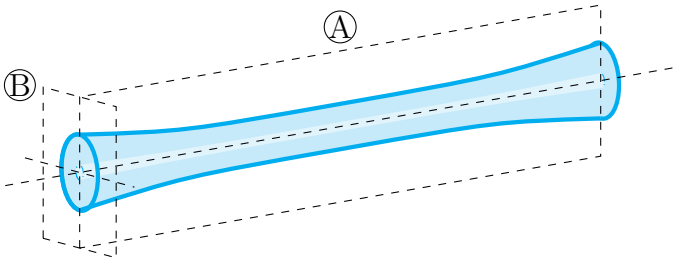

(a) 3D sketch of a deformed RDEA.

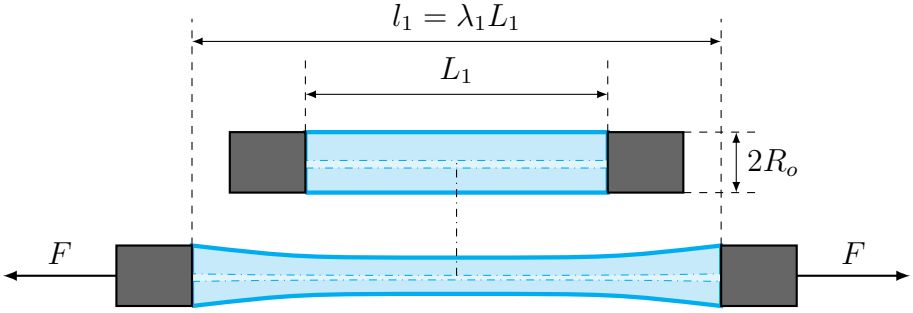

(b) Cross-section Ⓐ of a RDEA along the actuation direction (upper part: unloaded; lower part: axially loaded).

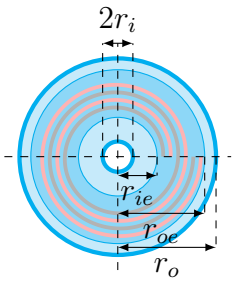

(c) Cross-section Ⓑ perpendicular to the actuation direction.

Figure 2: Sketch of a RDEA cross-section deforming under an axial load.

approximated by a combination of three hollow circles, as shown in Figure 3b. More specifically, the inner and outer hollow circles (denoted as a and c in Figure 3b) describe passive insulation regions, where no electrodes are present, while the intermediate hollow cylinder (denoted as b in Figure 3b) represents the electrically active material part.

Assumption 5. When the RDEA is activated via high voltage, it is assumed that an electric field E, directed along the radial direction, permeates the volume occupied by region b only.

Assumption 6. Passive regions a and c are modeled as three-dimensional hyperelastic solids, while active region b is modeled as a three-dimensional and electro-mechanically-coupled hyperelastic body. The electro-mechanical state in each one of the three regions is modeled in a lumped-parameter way, and described through the mean

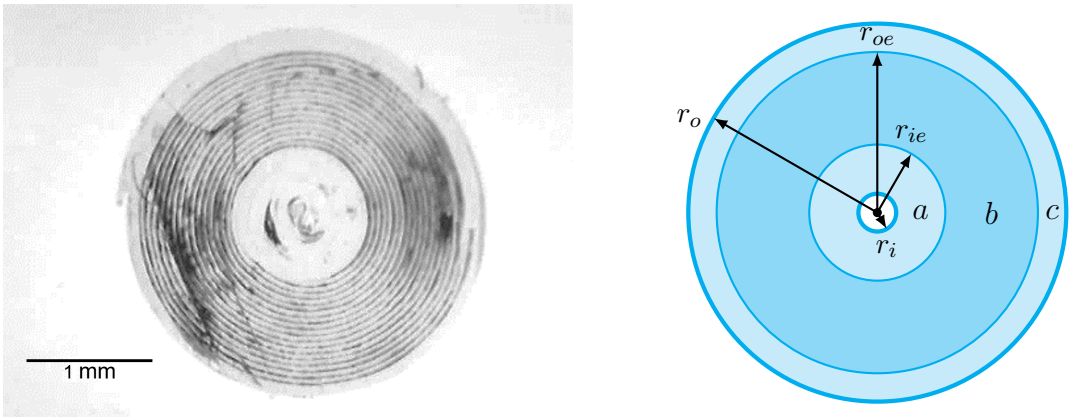

(a) Microscope picture of a RDEA specimen. (b) Sketch for the concentric cylinder model.

Figure 3: Side-by-side comparison of an actual RDEA specimen with the corresponding model geometry.

values of the stress, stretch, and electric field. Radial gradients within the single regions are neglected, whereas different mean stretches and stresses are used for each region.

Assumptions 1-5 reasonably hold true for thin and slender RDEAs, obtained from a tightly rolled membrane with an unwound thickness much smaller than the roll radius. Assumption 6 allows developing the model within a lumped-parameter, rather than a finite element, mathematical framework. On the one hand, this is highly desirable for numerically efficient dynamic simulations and real-time control applications. On the other hand, the fact that we are considering three separate regions still permits to account, at least at a first order, for the effects of radial inhomogeneities within the material due to the non-negligible passive regions.

Based on Figure 3b, we define the following quantities: R_i (r_i) is the inner radius of passive region a in undeformed (deformed) state; R_{ie} (r_{ie}) represents the inner radius of region b in undeformed (deformed) state; R_{oe} (r_{oe}) describes the outer radius of region b in undeformed (deformed) state; R_o (r_o) defines the outer radius of region c in undeformed (deformed) state. Note that capital letters are used to represent RDEA geometrical quantities in the undeformed configuration, while lowercase letters denote the geometry in the current configuration, respectively.

The state of deformation of each hollow cylinder is described by three principal stretches, i.e., an axial stretch λ_{1j} directed along the membrane thickness direction, a circumferential stretch λ_{2j}, and a radial stretch λ_{3j}, $j \in \{a, b, c\}$. Such principal stretches can be expressed as functions of the above defined geometric parameters, as follows:

$$\lambda_{1a} = \frac{l_1}{L_1} \qquad \lambda_{2a} = \frac{r_{ie} + r_i}{R_{ie} + R_i} \qquad \lambda_{3a} = \frac{r_{ie} - r_i}{R_{ie} - R_i} \tag{1}$$

$$\lambda_{1b} = \frac{l_1}{L_1} \qquad \lambda_{2b} = \frac{r_{oe} + r_{ie}}{R_{oe} + R_{ie}} \qquad \lambda_{3b} = \frac{r_{oe} - r_{ie}}{R_{oe} - R_{ie}} \tag{2}$$

$$\lambda_{1c} = \frac{l_1}{L_1} \qquad \lambda_{2c} = \frac{r_o + r_{oe}}{R_o + R_{oe}} \qquad \lambda_{3c} = \frac{r_o - r_{oe}}{R_o - R_{oe}}. \tag{3}$$

Note that stretches (1)-(3) represent averaged material quantities, and thus are independent of a specific spatial location.

In the following, we identify a number of relationships among the stretches in (1)-(3), and we impose kinematic constraints dictated by the physical problem, hence reducing the number of independent stretches needed for a complete description of the RDEA configuration.

Because the cylinders undergo the same axial elongation, the axial stretches are equal and can be represented through a single variable λ_1:

$$\lambda_{1a} = \lambda_{1b} = \lambda_{1c} = \lambda_1 = \frac{l_1}{L_1}. \tag{4}$$

Furthermore, the stretches defined in (1)-(3) must be such that the volumes Ω_a, Ω_b and Ω_c of the three cylinders stay constant upon stretching. Such volume preservation assumption is generally considered to hold true for elastomers, including DEs [1]. Prescribing volume preservation of the hollow cylinders leads to the following constraints:

$$\Omega_a = \pi(R_{ie}^2 - R_i^2)L_1 = \pi(r_{ie}^2 - r_i^2)l_1 \qquad \Rightarrow \qquad \lambda_{3a} = \frac{1}{\lambda_{1a}\lambda_{2a}}, \tag{5}$$

$$\Omega_b = \pi(R_{oe}^2 - R_{ie}^2)L_1 = \pi(r_{oe}^2 - r_{ie}^2)l_1 \qquad \Rightarrow \qquad \lambda_{3b} = \frac{1}{\lambda_{1b}\lambda_{2b}}, \tag{6}$$

$$\Omega_c = \pi(R_o^2 - R_{oe}^2)L_1 = \pi(r_o^2 - r_{oe}^2)l_1 \qquad \Rightarrow \qquad \lambda_{3c} = \frac{1}{\lambda_{1c}\lambda_{2c}}. \tag{7}$$

Finally, two additional conditions hold, which account for the fact that neighbouring regions remain in contact upon deformation. In particular, the following condition holds, which ensures that the outer radius of cylinder a coincides with the inner radius of cylinder b:

$$(R_{ie} + R_i)\lambda_{2a} + (R_{ie} - R_i)\lambda_{3a} - (R_{oe} + R_{ie})\lambda_{2b} + (R_{oe} - R_{ie})\lambda_{3b} = 0. \tag{8}$$

Equation (8) is obtained by extracting the values of r_{ie} (as a function of the stretches and the initial dimensions) for cylinder a and b respectively from (1) and (2), and equating them.

Similarly, the following relation holds, which guarantees the outer radius of b and the inner radius of c be equal:

$$(R_{oe} + R_{ie})\lambda_{2b} + (R_{oe} - R_{ie})\lambda_{3b} - (R_o + R_{oe})\lambda_{2c} + (R_o - R_{oe})\lambda_{3c} = 0. \tag{9}$$

In analogy to the previous case, equation (9) is obtained by extracting the values of r_{oe} for cylinder b and c respectively from (2) and (3), and equating them.

By collecting (4)-(9), a total of 7 conditions is obtained among the 9 stretches defined in (1)-(3). Note how (4)-(7) can be directly used to eliminate 5 out of the 9 free stretches. However, (8) and (9) cannot be uniquely solved in an analytic way, once λ_{3a}, λ_{3b}, and λ_{3c} are replaced. As a result, we treat them as independent constraints in the subsequent free-energy formulation.

For future convenience, we hereby introduce the volume ratios of the single cylinders over the total material volume:

$$\eta_a = \frac{\Omega_a}{\Omega} = \frac{\pi(R_{ie}^2 - R_i^2)L_1}{\pi(R_o^2 - R_i^2)L_1} = \frac{R_{ie}^2 - R_i^2}{R_o^2 - R_i^2} \tag{10}$$

$$\eta_b = \frac{\Omega_b}{\Omega} = \frac{\pi(R_{oe}^2 - R_{ie}^2)L_1}{\pi(R_o^2 - R_i^2)L_1} = \frac{R_{oe}^2 - R_{ie}^2}{R_o^2 - R_i^2} \tag{11}$$

$$\eta_c = \frac{\Omega_c}{\Omega} = \frac{\pi(R_o^2 - R_{oe}^2)L_1}{\pi(R_o^2 - R_i^2)L_1} = \frac{R_o^2 - R_{oe}^2}{R_o^2 - R_i^2}. \tag{12}$$

From (10)-(12), it directly follows that $\eta_a + \eta_b + \eta_c = 1$. Additionally, we define the electrical correction factor α_{e1} as follows

$$\alpha_{e1} = \frac{L_{1e}}{L_1}, \tag{13}$$

where L_{1e} represents the unstretched length of the DE electrode along the axis, with $L_{1e} \leq L_1$. Quantity α_{e1} describes the relative portion of roll axis which is covered by the electrodes.

In the following, we derive the model constitutive equations using a free-energy approach. For simplicity, we start by neglecting irreversible phenomena which are due to losses in the DE material (a more in-depth discussion on this aspect is postponed to Section 3.5). For a conservative and isothermal system, the internal virtual work given as the variation of the Helmholtz free-energy $d\Psi$ is equal to the external virtual work δW performed on the system:

$$d\Psi = \delta W = F\delta l_1 + v\delta q. \tag{14}$$

The total external work, described by the right hand-side of (14), consists of the sum of a mechanical (first term) and an electrostatic (second term) contributions. The considered generalized external forces are the force F, directed along the actuation (i.e., axial) direction, and the voltage v applied to the RDEA electrodes. The corresponding conjugated virtual displacements are the virtual actuator length variation δl_1 and the virtual charge displacement δq.

Next, we introduce the following normalized quantities:

$$\psi = \frac{\Psi}{\Omega} = \frac{\Psi}{\pi(R_o^2 - R_i^2)L_1}, \tag{15}$$

$$\sigma_1 = \frac{F}{\pi\left(r_o^2 - r_i^2\right)} = \frac{\lambda_1}{\pi\left(R_o^2 - R_i^2\right)}F, \tag{16}$$

$$N = \frac{r_{oe} - r_{ie}}{l_3} = \frac{R_{oe} - R_{ie}}{L_3}, \tag{17}$$

$$E = \frac{v}{l_3} = \frac{\lambda_1\lambda_{2b}N}{R_{oe} - R_{ie}}v, \tag{18}$$

$$D = \frac{q}{NA_{avg}} = \frac{1}{N\alpha_{e1}L_1\pi(R_{oe} + R_{ie})\lambda_1\lambda_{2b}}q, \tag{19}$$

where: ψ is the Helmholtz free-energy density; σ_1 is an average stress (or, more appropriately, an average force density) along the axial direction; N is the number of turns in the region b of the roll, and L_3 and l_3 are the nominal and actual thickness of a single layer (note how Assumption 2 implies that N is constant and uniquely defined, regardless of the considered configuration); E is the current averaged field strength inside the active region b, directed along the radial direction; D is the average electrical displacement, computed as the total charge on the electrodes divided by the product between number of active layers N in region b and average electrode surface area A_{avg}.

By replacing (4), (10)-(12), and (15)-(19) in (14), we obtain the following normalized version of the principle of virtual work:

$$d\psi = \left(\frac{\sigma_1 + \alpha_{e1}\eta_b ED}{\lambda_1}\right)\delta\lambda_1 + \alpha_{e1}\eta_b\frac{ED}{\lambda_{2b}}\delta\lambda_{2b} + \alpha_{e1}\eta_b E\delta D. \tag{20}$$

The Helmholtz free-energy density is modeled as follows:

$$\begin{aligned}\psi(\lambda_1, \lambda_{2a}, \lambda_{2b}, \lambda_{2c}, D, p_1, p_2) = {} & \eta_a\psi_m(\lambda_1, \lambda_{2a}) + \eta_b\psi_m(\lambda_1, \lambda_{2b}) + \eta_c\psi_m(\lambda_1, \lambda_{2c}) \\ & + \alpha_{e1}\eta_b\psi_e(D) + p_1c_1(\lambda_1, \lambda_{2a}, \lambda_{2b}) + p_2c_2(\lambda_1, \lambda_{2b}, \lambda_{2c}).\end{aligned} \tag{21}$$

In principle, ψ shall explicitly depend on the independent order parameters of the system only, i.e., a minimum set of stretches together with the electrical displacement. As remarked above, five out of the nine stretches stretches defined by (1)-(3) can be eliminated by solving (4)-(7). However, since (8)-(9) cannot be solved unambiguously, we let ψ explicitly depend on the remaining four stretches λ_1, λ_{2a}, λ_{2b}, and λ_{2c}, and account for constraints (8)-(9) by introducing Lagrange multipliers p_1 and p_2 as further variables of ψ. Clearly, the electrical displacement D also represents a further independent variable on which ψ must depend.

The meaning of the different contributions on the right-hand side of (21) is discussed in the following. First, ψ_m denotes a generic hyperelastic free-energy density function, which depends on stretches λ_1 and λ_{2j}, $j \in \{a, b, c\}$. Therefore, the first three terms on the right-hand side of (21) can be interpreted as the elastic energy stored in the hollow cylinders a, b, and c, respectively. Different hyperelastic models are available from the

literature to characterize ψ_m [37, 38, 39]. In this work, we describe ψ_m by means of a Yeoh free-energy density [36]:

$$\psi_m(\lambda_1, \lambda_{2j}) = \sum_{i=1}^{3} C_{i0} \left(\lambda_1^2 + \lambda_{2j}^2 + \lambda_1^{-2}\lambda_{2j}^{-2} - 3\right)^i, \quad j \in \{a, b, c\}, \tag{22}$$

where C_{i0}, $i \in \{1, 2, 3\}$, represent constitutive material parameters. Function ψ_e models the electrostatic free-energy density of the RDEA, associated with the electric field E within active region b [38, 36]:

$$\psi_e(D) = \frac{D^2}{2\epsilon_0\epsilon_r}, \tag{23}$$

where ϵ_0 and ϵ_r are the vacuum and DE relative permittivities, respectively. The last two terms are introduced in the energy to model constraints (8) and (9), where:

$$c_1(\lambda_1, \lambda_{2a}, \lambda_{2b}) = (R_{ie} + R_i)\lambda_{2a} + (R_{ie} - R_i)\frac{1}{\lambda_1\lambda_{2a}} - (R_{oe} + R_{ie})\lambda_{2b} + (R_{oe} - R_{ie})\frac{1}{\lambda_1\lambda_{2b}} = 0 \tag{24}$$

and

$$c_2(\lambda_1, \lambda_{2b}, \lambda_{2c}) = (R_{oe} + R_{ie})\lambda_{2b} + (R_{oe} - R_{ie})\frac{1}{\lambda_1\lambda_{2b}} - (R_e + R_{oe})\lambda_{2c} + (R_e - R_{oe})\frac{1}{\lambda_1\lambda_{2c}} = 0. \tag{25}$$

The variation of ψ is given by

$$\begin{aligned}
&d\psi(\lambda_1, \lambda_{2a}, \lambda_{2b}, \lambda_{2c}, D, p_1, p_2) \\
&\quad= \left(\eta_a \frac{\partial \psi_m(\lambda_1, \lambda_{2a})}{\partial \lambda_1} + \eta_b \frac{\partial \psi_m(\lambda_1, \lambda_{2b})}{\partial \lambda_1} + \eta_c \frac{\partial \psi_m(\lambda_1, \lambda_{2c})}{\partial \lambda_1}\right. \\
&\qquad\qquad \left. + p_1 \frac{\partial c_1(\lambda_1, \lambda_{2a}, \lambda_{2b})}{\partial \lambda_1} + p_2 \frac{\partial c_2(\lambda_1, \lambda_{2b}, \lambda_{2c})}{\partial \lambda_1}\right) \delta\lambda_1 \\
&\qquad\qquad + \left(\eta_a \frac{\partial \psi_m(\lambda_1, \lambda_{2a})}{\partial \lambda_{2a}} + p_1 \frac{\partial c_1(\lambda_1, \lambda_{2a}, \lambda_{2b})}{\partial \lambda_{2a}}\right) \delta\lambda_{2a} \\
&\quad + \left(\eta_b \frac{\partial \psi_m(\lambda_1, \lambda_{2b})}{\partial \lambda_{2b}} + p_1 \frac{\partial c_1(\lambda_1, \lambda_{2a}, \lambda_{2c})}{\partial \lambda_{2b}} + p_2 \frac{\partial c_2(\lambda_1, \lambda_{2b}, \lambda_{2c})}{\partial \lambda_{2b}}\right) \delta\lambda_{2b} \\
&\qquad\qquad + \left(\eta_c \frac{\partial \psi_m(\lambda_1, \lambda_{2c})}{\partial \lambda_{2c}} + p_2 \frac{\partial c_2(\lambda_1, \lambda_{2b}, \lambda_{2c})}{\partial \lambda_{2c}}\right) \delta\lambda_{2c} \\
&\qquad + \left(\alpha_{e1}\eta_b \frac{D}{\epsilon_0\epsilon_r}\right) \delta D + c_1(\lambda_1, \lambda_{2a}, \lambda_{2b})\delta p_1 + c_2(\lambda_1, \lambda_{2b}, \lambda_{2c})\delta p_2.
\end{aligned} \tag{26}$$

The analytical expression of the partial derivatives of ψ_m, c_1, and c_2 is omitted from (26) for conciseness. By replacing (20) in (26), and equating the terms multiplying the

same virtual displacements, we obtain the following model:

$$\begin{cases} \sigma_1 = \eta_a \dfrac{\partial \psi_m(\lambda_1, \lambda_{2a})}{\partial \lambda_1} + \eta_b \dfrac{\partial \psi_m(\lambda_1, \lambda_{2b})}{\partial \lambda_1} + \eta_c \dfrac{\partial \psi_m(\lambda_1, \lambda_{2c})}{\partial \lambda_1} \\ \qquad + p_1 \dfrac{\partial c_1(\lambda_1, \lambda_{2a}, \lambda_{2b})}{\partial \lambda_1} + p_2 \dfrac{\partial c_2(\lambda_1, \lambda_{2b}, \lambda_{2c})}{\partial \lambda_1} - \alpha_{e1} \eta_b \epsilon_0 \epsilon_r E^2 \\ 0 = \eta_a \dfrac{\partial \psi_m(\lambda_1, \lambda_{2a})}{\partial \lambda_{2a}} + p_1 \dfrac{\partial c_1(\lambda_1, \lambda_{2a}, \lambda_{2b})}{\partial \lambda_{2a}} \\ 0 = \eta_b \dfrac{\partial \psi_m(\lambda_1, \lambda_{2b})}{\partial \lambda_{2b}} + p_1 \dfrac{\partial c_1(\lambda_1, \lambda_{2a}, \lambda_{2c})}{\partial \lambda_{2b}} + p_2 \dfrac{\partial c_2(\lambda_1, \lambda_{2b}, \lambda_{2c})}{\partial \lambda_{2b}} - \alpha_{e1} \eta_b \epsilon_0 \epsilon_r E^2 \\ 0 = \eta_c \dfrac{\partial \psi_m(\lambda_1, \lambda_{2c})}{\partial \lambda_{2c}} + p_2 \dfrac{\partial c_2(\lambda_1, \lambda_{2b}, \lambda_{2c})}{\partial \lambda_{2c}} \\ 0 = c_1(\lambda_1, \lambda_{2a}, \lambda_{2b}) \\ 0 = c_2(\lambda_1, \lambda_{2b}, \lambda_{2c}) \end{cases}. \tag{27}$$

Model (27) consists of a set of 6 independent algebraic equations. Given λ_1 and E, the system can be solved for variables σ_1, λ_{2a}, λ_{2b}, λ_{2C}, p_1, and p_2. Once a solution for (27) is obtained, l_1, F, v can be calculated from the corresponding λ_1, σ_1, E by means of equations (4), (16), and (18).

To complement model (27), a consistent expression for the electrical capacitance of the RDEA can be found. We first express v from Ψ as follows:

$$v = \frac{\partial \Psi}{\partial q} = \Omega \frac{\partial \psi}{\partial D} \frac{\partial D}{\partial q} = \frac{L_3^2}{\epsilon_0 \epsilon_r \alpha_{e1} L_1 \pi \left({R_{oe}}^2 - {R_{ie}}^2 \right)} \frac{1}{\lambda_1^2 \lambda_{2b}^2} q. \tag{28}$$

Based on (28), the electrical capacitance can be computed as follows:

$$C(\lambda_1, \lambda_{2b}) = \frac{\partial q}{\partial v} = \epsilon_0 \epsilon_r \alpha_{e1} \frac{L_1 \pi \left({R_{oe}}^2 - {R_{ie}}^2 \right)}{{L_3}^2} \lambda_1^2 \lambda_{2b}^2 = C_0 \lambda_1^2 \lambda_{2b}^2, \tag{29}$$

where C_0 denotes the capacitance of the undeformed RDEA. Since it is mainly constructed starting from the three-ring assumption, the RDEA model described by (27) and (29) will be hereafter referred to as 3R (three-ring) model.

The presented 3R model permits to effectively describe the behavior of a slender and tightly rolled RDEA in a lumped-parameter fashion. Nonetheless, because it comes in the form of a nonlinear system of six algebraic equations (cf. (27)), its practical solution may turn out to be numerically expensive, especially for real-time control applications. To overcome this issue, in the following we propose two simplified versions of the RDEA model, which might suitably and conveniently replace the 3R model under specific assumptions.

3.2. RDEA Lumped-Parameter Model 2: One-Ring (1R)

A first possible way to simplify the 3R model comes in the form of the following additional assumption.

Assumption 7. Each one of the three rings describing the RDEA cross-section in Figure 3b is characterized by the same amount of circumferential stretch.

The above assumption prescribes a further degree of homogeneity within the material, whose validity might depend on several factors (a more in-depth analysis will be presented in Section 3.4). When considered all together, Assumptions 1-7 imply that the three rings of material can be described by a unique set of principal stretches, i.e., the RDEA uniformly deforms as a single hollow cylinder. Mathematically, Assumption 7 implies that continuity constraints (8)-(9) are replaced with the following one

$$\lambda_{2a} = \lambda_{2b} = \lambda_{2c} = \lambda_2. \tag{30}$$

Note that (30), in conjunction with relationship (4)-(7), permits to directly eliminate 7 of the 9 principal stretches, and express all of them as functions of λ_1 and λ_2 explicitly.

By repeating the energy treatment of Section 3.1, and replacing constraints (8)-(9) with the new condition (30), the normalized version of the principle of virtual work (14) becomes:

$$d\psi = \left(\frac{\sigma_1 + \alpha_{e1}\eta_b E D}{\lambda_1}\right)\delta\lambda_1 + \alpha_{e1}\eta_b \frac{ED}{\lambda_2}\delta\lambda_2 + \alpha_{e1}\eta_b E\delta D. \tag{31}$$

Based on (30), we can further reformulate the Helmholtz free-energy density in (21) through the following expression:

$$\psi(\lambda_1, \lambda_2, D) = \psi_m(\lambda_1, \lambda_2) + \alpha_{e1}\eta_b\psi_e(D). \tag{32}$$

Since in this case it is possible to solve constraints (30) analytically, the free-energy density can be directly expressed as a function of the independent stretches λ_1 and λ_2 only, alongside with D. Consequently, the Lagrange multipliers do no longer need to be introduced.

By differentiating (32), replacing it into (31), and repeating the steps previously outlined in Section 3.1, the constitutive equations of the resulting model can be computed as follows:

$$\begin{cases} \sigma_1 = \lambda_1 \dfrac{\partial\psi_m(\lambda_1, \lambda_2)}{\partial\lambda_1} - \alpha_{e1}\eta_b\epsilon_0\epsilon_r E^2 \\ 0 = \lambda_2 \dfrac{\partial\psi_m(\lambda_1, \lambda_2)}{\partial\lambda_2} - \alpha_{e1}\eta_b\epsilon_0\epsilon_r E^2. \end{cases} \tag{33}$$

Note that (33) consists of a set of two nonlinear equations, which can be uniquely solved for σ_1 and λ_2 once λ_1 and E are given as inputs. The resulting system turn out to be significantly simpler to tackle numerically, compared to (27).

Finally, the capacitance equation for this model can be easily derived by replacing (30) in (29), leading to:

$$C(\lambda_1, \lambda_2) = \epsilon_0\epsilon_r\alpha_{e1}\frac{L_1\pi\left({R_{oe}}^2 - {R_{ie}}^2\right)}{{L_3}^2}\lambda_1^2\lambda_2^2 = C_0\lambda_1^2\lambda_2^2. \tag{34}$$

By using an argument similar to the one in Section 3.3, the model described by (33) and (34) will be referred to as one-ring (1R) model (since this time the three rings

deform as a single hollow cylinder, whose behavior follows equation (33)). Note how model (33) is formally identical to the one for strip-shaped DE membranes previously derived in [36].

3.3. RDEA Lumped-Parameter Model 3: Strongly Uniaxial (SU)

A potential way to further simplify the 3R model is outlined in the following. For a homogeneous hollow cylinder, such as the one used to approximate the shape of the RDEA, the inner and outer radii (i.e., r_i and r_o) are allowed to change independently upon loading. In contrast, if we consider a solid cylinder, its inner radius would remain unchanged, i.e., $r_i = R_i = 0$ all the time. If this is the case, it can readily be verified that the principal stretches of the resulting cylinder would also satisfy the following symmetry condition

$$\lambda_2 = \lambda_3. \tag{35}$$

Following this reasoning, we can assume that, if the inner passive region of the RDEA a is sufficiently thick in comparison to the active one, it will contrast changes in r_i. As a result, it can be assumed that the RDEA will deform in a similar fashion to a solid cylinder, rather than an unconstrained hollow one. This fact can be formalized with the following additional assumption.

Assumption 8. The RDEA deforms in such a way that the circumferential and radial stretches are always equal, regardless of the applied electro-mechanical load.

While this assumption adds on to the previous assumptions of the 1R model, and reduces the number of degrees of freedom of the problem, it provides a means for implicitly taking into account the constraint to radial electrically-induced expansions created by the passive regions. By describing the RDEA as an equivalent unconstrained DE strip, the 1R model fails to account for the large radial stiffness generated by thick inner passive regions, which expectedly leads towards a response similar to that of a full cylinder.

By considering Assumption 8 alongside with Assumptions 1-7 and incompressibility conditions (5)-(7), the following additional constraints are obtained

$$\lambda_{2a} = \lambda_{2b} = \lambda_{2c} = \lambda_2 = \frac{1}{\sqrt{\lambda_1}}. \tag{36}$$

Collecting together (4)-(7) and (36), all the 9 principal stretches can be analytically expressed as a function of λ_1 only.

By considering the new set of constraints for the stretches, we can rewrite the normalized version of the principle of virtual work (14) as follows:

$$d\psi = \left(\frac{\sigma_1 + 0.5\alpha_{e1}\eta_b E D}{\lambda_1} \right) \delta\lambda_1 + \alpha_{e1}\eta_b E \delta D, \tag{37}$$

while the Helmholtz free-energy density (21) becomes

$$\psi(\lambda_1, D) = \psi_m(\lambda_1, \lambda_2(\lambda_1)) + \alpha_{e1}\eta_b \psi_e(D), \tag{38}$$

where $\lambda_2(\lambda_1)$ is given by (36). Note that, in this case, it is possible to let the free-energy density (38) explicitly depend on the only independent stretch λ_1 and on D, without using additional Lagrange multipliers.

The differentiation of (38), together with the subsequent comparison with (37), allows us to obtain the following constitutive equation:

$$\sigma_1 = \lambda_1 \left(\frac{\partial \psi_m(\lambda_1, \lambda_2(\lambda_1))}{\partial \lambda_1} + \frac{\partial \psi_m(\lambda_1, \lambda_2(\lambda_1))}{\partial \lambda_2(\lambda_1)} \frac{\partial \lambda_2(\lambda_1)}{\partial \lambda_1} \right) - 0.5 \alpha_{e1} \eta_b \epsilon_0 \epsilon_r E^2, \tag{39}$$

where λ_2 depends on λ_1 according to (36), and

$$\frac{\partial \lambda_2(\lambda_1)}{\partial \lambda_1} = -\frac{1}{2\lambda_1 \sqrt{\lambda_1}}. \tag{40}$$

Note that λ_1 and $\lambda_2(\lambda_1)$ must be treated as independent variables when computing the partial derivatives of ψ_m in (39). Equation (39) can be readily solved for σ_1, once λ_1 and E are known. A remarkable difference between (39) and models (27) and (33) (i.e., 3R and 1R, respectively) is the factor 0.5 which multiplies the E-dependent Maxwell stress. This is a direct consequence of the additional kinematic constraint given by (36).

The capacitance can be then computed by simply replacing (36) into (29), leading to

$$C(\lambda_1) = \epsilon_0 \epsilon_r \alpha_{e1} \frac{L_1 \pi \left({R_{oe}}^2 - {R_{ie}}^2 \right)}{{L_3}^2} \lambda_1 = C_0 \lambda_1. \tag{41}$$

Remarkably, a linear dependency between axial stretch and capacitance is observed in this case.

Note that (36) is generally referred to as uniaxial condition in the literature [36, 37]. It is also simple to prove that the 1R model (33) satisfies condition (36) only when $E = 0$. In contrast, model (39) enforces (36) by construction, regardless of the applied electric field. For this reason, model (39) will be henceforth referred to as strongly uniaxial (SU) model.

3.4. Model Comparison

The main differences among the three models introduced in Sections 3.1-3.3 can be summarized as follows:

- *3R model*: it is described by equations (27) and (29), and is based on Assumptions 1-6. It is constructed by considering that the RDEA behaves as the combination of three different hollow cylinders;
- *1R model*: it is described by equations (33) and (34), and is based on Assumptions 1-7. It is constructed by considering that the RDEA behaves as a single, lumped hollow cylinder;
- *SU model*: it is described by equations (39) and (41), and is based on Assumptions 1-8. It is constructed by considering that the RDEA behaves as a single, lumped full cylinder.

In this section, we conduct a comparative study between the three models, based on realistic material and geometric parameters. The aim is to understand the conditions for which the simpler models (1R and SU) tightly approximate the behavior of the more complex one (3R). Such analysis will play a critical role for the selection of the best RDEA model, which accounts for an optimal trade-off between complexity and numerical accuracy.

To perform the above mentioned comparison, the following case study is considered. The material parameters are chosen according to the experimental investigation in [36], namely $C_{10} = 241\,\text{kPa}, C_{20} = -33.2\,\text{kPa}, C_{30} = 20.1\,\text{kPa}$, and $\epsilon_r = 2.8$, while $L_3 = 48$ μm and $\alpha_{e1} = 1$ for simplicity. Three different rolls are considered in this study, each one of them representing different extreme cases, by properly selecting the values of the radii as follows: hollow inner core, corresponding to $R_i = 0.86\,\text{mm}$, $R_{ie} = 0.88\,\text{mm}$, $R_{oe} = 1.76\,\text{mm}$, and $R_o = 1.8\,\text{mm}$; active inner core, corresponding to $R_i = 0\,\text{mm}$, $R_{ie} = 0.088\,\text{mm}$, $R_{oe} = 1.76\,\text{mm}$, and $R_o = 1.8\,\text{mm}$; passive inner core, corresponding to $R_i = 0\,\text{mm}$, $R_{ie} = 0.81\,\text{mm}$, $R_{oe} = 1.76\,\text{mm}$, and $R_o = 1.8\,\text{mm}$. By analyzing those configurations, we can understand the role of the inner core in determining the RDEA electro-mechanical response.

The response of each one of those cases is first simulated by means of the 3R model. The results are shown in Figure 4a for the hollow core RDEA, in Figure 4b for the active core RDEA, and in Figure 4c for the passive core RDEA, respectively. Each picture shows the simulated cross-section in three different situations, i.e., unloaded ($\lambda_1 = 1$, $v = 0$ V) on the left-hand side, mechanically loaded ($\lambda_1 = 1.75$, $v = 0$ V) on the upper-right hand side, and electro-mechanically loaded ($\lambda_1 = 1.75$, $v = 3.5$ kV) on the lower-right hand side. In the case of the RDEA with hollow core, shown in Figure 4a, the mechanical loading leads to a reduction in both inner and outer radii, while the application of an electric field causes both of them to expand again. This behavior is somehow expected, and also similar to the one of conventional strip-shaped DE membranes.

When we consider a RDEA whose active part covers almost the entirety of the material volume, as in Figure 4b, some differences with respect to the previous case are visible. When stretching the RDEA, the outer radius contracts significantly. However, when an electric field is also applied, the RDEA geometry remains practically unchanged. In this scenario, as both R_i and R_{ie} tend to 0, circumferential and radial stretches λ_2 and λ_3 are equal in each portion of the RDEA, as a consequence of constraints (8) and (9), and the roll behaves as a single solid uniaxial cylinder. A similar behavior is also observed in case of the RDEA with passive core, reported in Figure 4c. Based on such analysis, we understand that the parameter which determines the RDEA deformation kinematics upon electrical activation is mostly the inner radius R_i, rather than the size of inner passive region $R_{ie} - R_i$. In particular, the closer R_i to 0, the less the RDEA is free to undergo an unconstrained deformation when subject to an electric field.

A quantitative comparison between 3R and the two simplified models is then

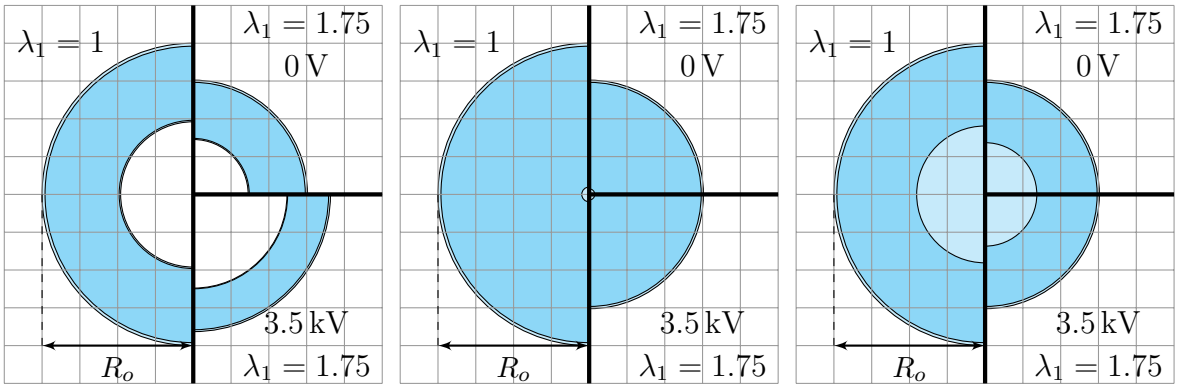

(a) Hollow core. (b) Active core. (c) Passive core.

Figure 4: Comparison of cross-sections for different geometries in loaded/unloaded configurations and at different voltages according to the 3R model. For this comparison, the radii are chosen as follows: hollow core (a) corresponds to $R_i = 0.86\,\text{mm}$, $R_{ie} = 0.88\,\text{mm}$, $R_{oe} = 1.76\,\text{mm}$, and $R_o = 1.8\,\text{mm}$; active core (b) corresponds to $R_i = 0\,\text{mm}$, $R_{ie} = 0.088\,\text{mm}$, $R_{oe} = 1.76\,\text{mm}$, and $R_o = 1.8\,\text{mm}$; passive core (c) corresponds to $R_i = 0\,\text{mm}$, $R_{ie} = 0.81\,\text{mm}$, $R_{oe} = 1.76\,\text{mm}$, and $R_o = 1.8\,\text{mm}$.

performed, in order to understand the domain of validity of the additional assumptions which are introduced. The numerical comparison is shown in Figure 5 for the hollow core case (corresponding to Figure 4a), in Figure 6 for the active core case (corresponding to Figure 4b), and in Figure 7 for the passive core case (corresponding to Figure 4c), respectively. Each plot shows the circumferential stretches λ_2 (upper part) and the axial stresses σ_1 (center part) computed as a function of λ_1 for the three models, together with the stress errors e_{σ_1} between the simplified and 3R model (lower part), for both $v = 0$ V (left-hand side) and $v = 3.5$ kV (right hand-side) cases. In all the cases, the 3R model results are represented in black, while the 1R and SU are depicted in blue and red, respectively.

First, we analyze the results corresponding to the hollow core case, shown in Figure 5. For the $v = 0$ V case, all models have coincident circumferential stretches. This result is somehow expected, since uniaxiality is assumed to hold for a pure tensile test conducted on a thin and slender roll. As a result, also the stresses predicted by the three models are practically identical. When comparing the curves computed for $v = 3.5$ kV, on the other hand, a remarkable difference is observed among the three models. First, one can note how the circumferential stretches deviate remarkably. The 1R model provides an accurate approximation of the circumferential stretch of the active region of the 3R model, i.e., λ_{2b}, reasonably due to the small thickness of the passive regions. The stretch predictions of the SU model, on the other hand, significantly deviate from the 3R model. As a direct result, the stress predicted by the 1R model approximates much more tightly the stress of the 3R, while the SU model is affected by a maximum

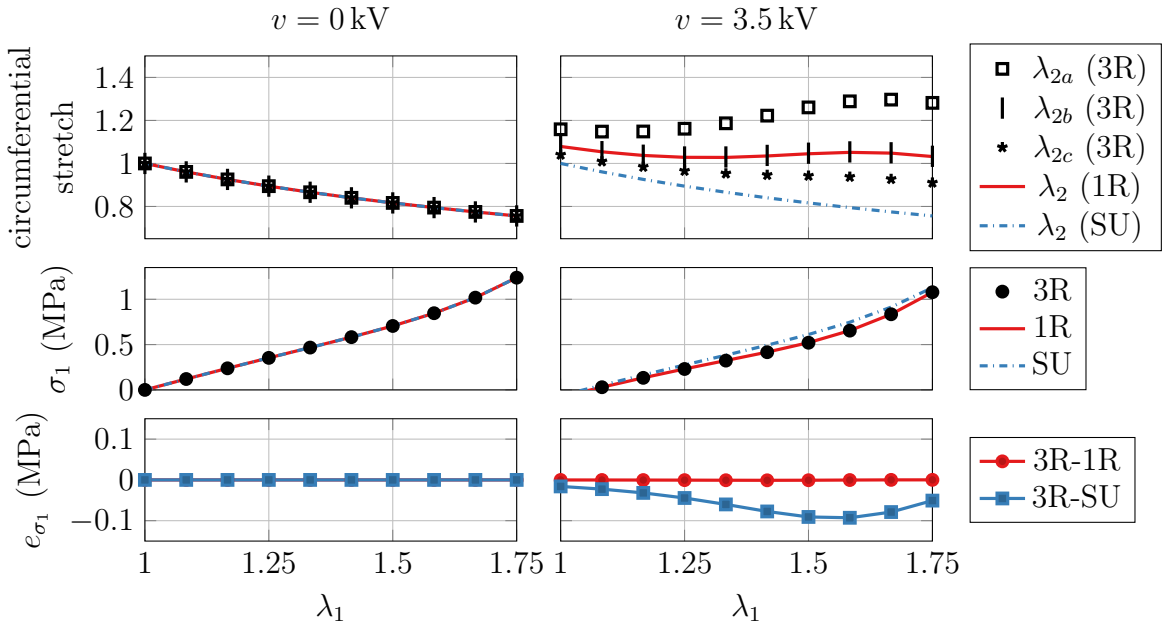

Figure 5: Model comparison, hollow core.

error of 0.1 MPa over a range of 1 MPa. The situation appears remarkably different if we analyze the results for the RDEA with active core, shown in Figure 6. The plots for the case $v = 0$ V appear identical to Figure 5, thus implying that uniaxiality still holds true. Quite remarkably, the results obtained for $v = 3.5$ kV suggest a strong agreement between 3R and SU models, both in terms of circumferential stretches and stress. As expected, the 1R model turns out to be inaccurate in this case. Note how this model predicts a circumferential expansion, which cannot occur in reality. If such an expansion occurred, the stretches in the central portion of the core would in fact tend to infinity. Such a misprediction of λ_2 leads to stress errors on the order of 0.1 MPa. Qualitatively similar results are also obtained for the RDEA with the passive core, shown in Figure 7. The only difference is given by the value of the stress error for the 1R model, which has now a peak value on the order of 0.055 MPa.

The conducted analysis confirms that parameter R_i plays a crucial role for determining whether the 3R model can or cannot be approximated by the 1R and SU models. For very small values of R_i, ideally close to 0, the SU behaves identically to the 3R. In this case, the SU model represents then the best trade-off between complexity and accuracy. For values of R_i closer to R_o, the 3R model is better approximated by the 1R one, which can then be considered as the optimal modeling choice. Furthermore, the value of R_{ie} seems not to play a relevant role in determing the stretch behavior, but has an effect on the absolute stress error. Naturally, the conducted analysis only covers extreme cases, and several intermediate situations could manifest for other geometries. As an example, Figure 8 shows the force error computed by choosing $R_i \in \{0.1, 0.2, \ldots, 0.9\} \cdot R_{ie}$, by considering $R_{ie} = 0.6\,\mathrm{mm}$, $R_{oe} = 1.21\,\mathrm{mm}$, and $R_o = 1.33\,\mathrm{mm}$. As it can be seen, decreasing R_i induces a smooth transition from the

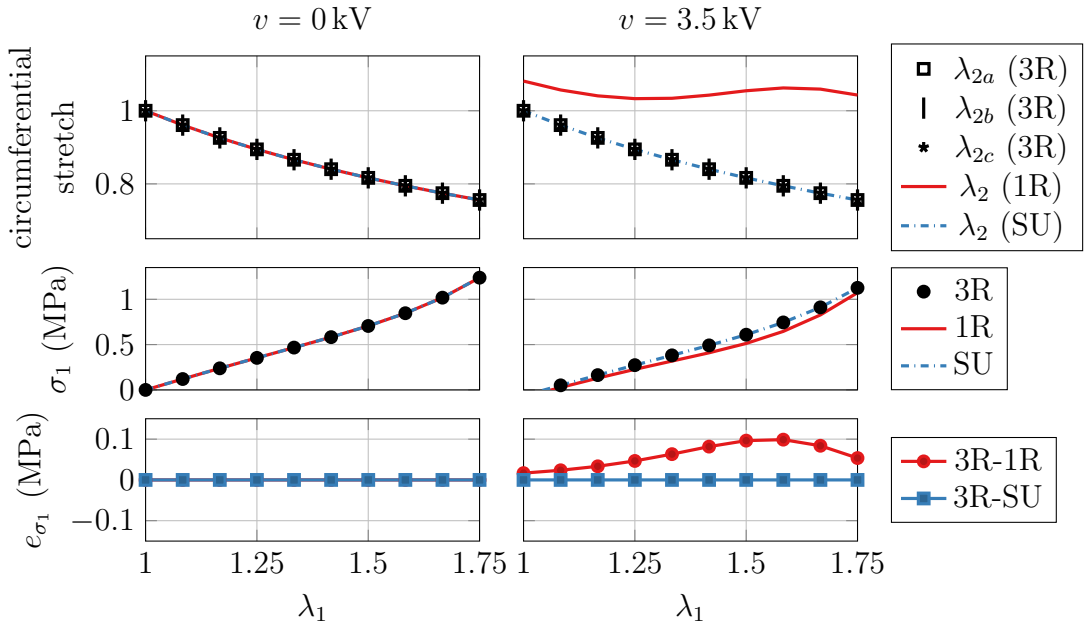

Figure 6: Model comparison, active core.

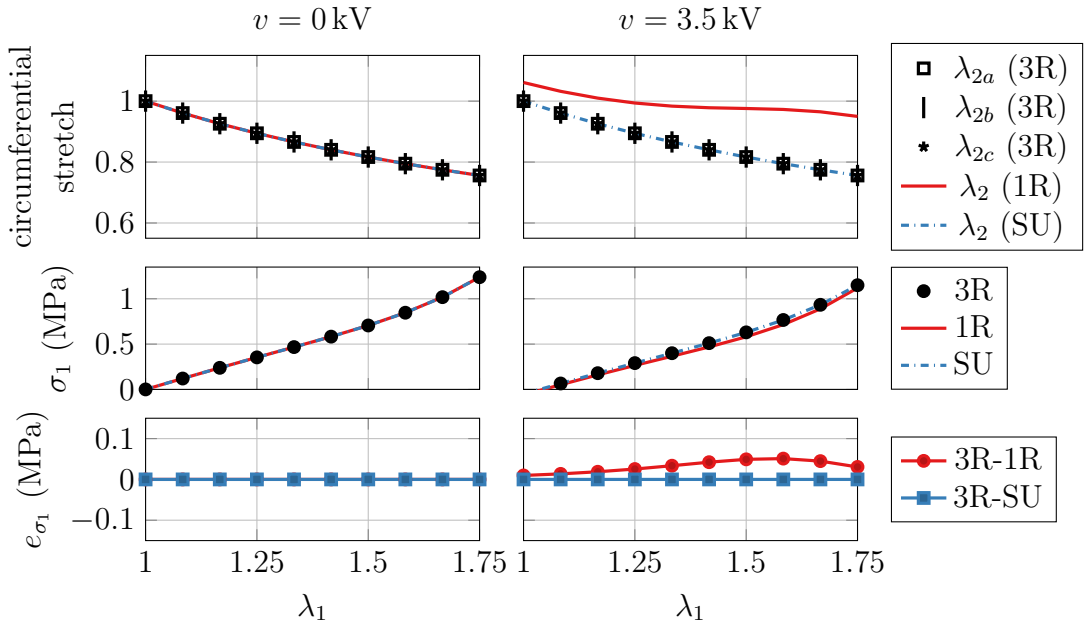

Figure 7: Model comparison, passive core.

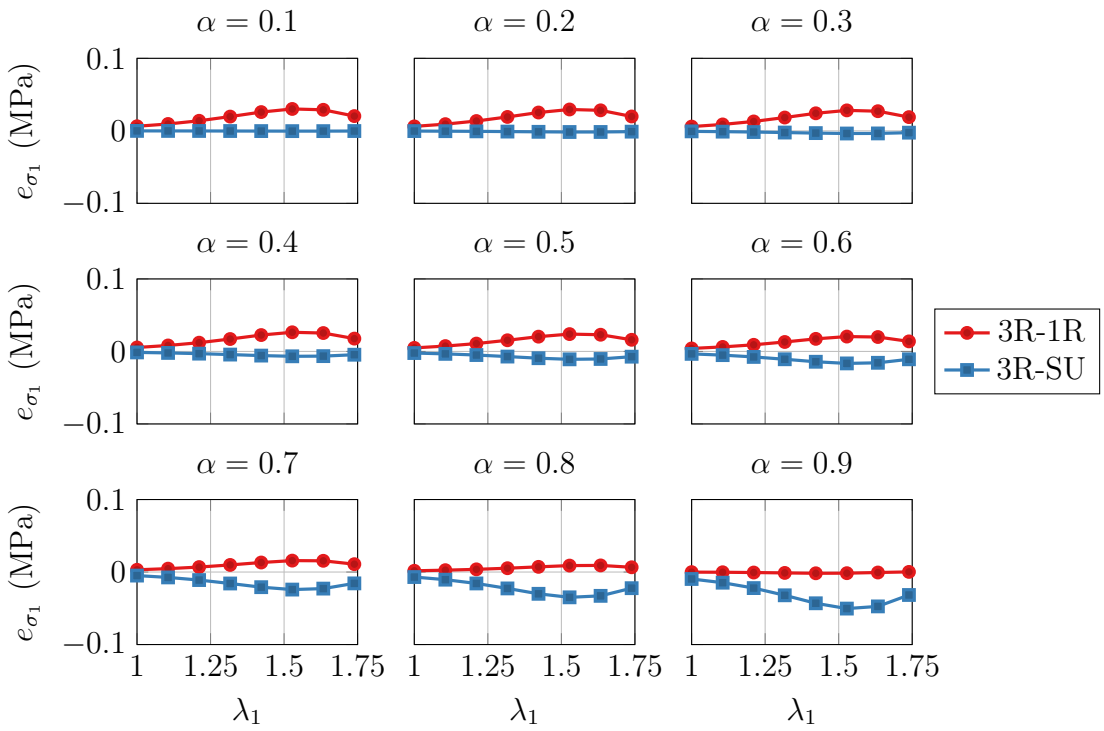

Figure 8: Deviations of the predicted average stress σ_1 of the two simplified models (1R in red, SU in blue) in comparison to the 3R model, for a sweep of $R_i \in \{0.1, 0.2, \ldots, 0.9\} \cdot R_{ie}$.

1R behavior to the SU one, with values in between for which none of the approximations accurately describe the 3R model.

As a final note, we point out that the proportions of the reference geometry used for the passive core case (i.e., the one shown in Figure 4c and Figure 7) closely resembles the one of the real-life RDEA prototypes investigated in the next section. Therefore, we conclude that the SU model represents the most appropriate choice for the analysis of the prototypes under investigation.

3.5. Inclusion of Viscoelastic Effects

All the modeling considerations in Sections 3.1-3.4 are based on the assumption that the DE behaves as a reversible transducers, i.e., no dissipations occur in the material. This reflects in the considered form (14) of the principle of virtual work, which states that all the work done on the DE is stored as free-energy. In reality, however, DE transducers exhibit irreversibilities which are mostly due to viscoelastic processes within the material. While those effects are practically negliglible under quasi-static loading conditions, they become relevant in dynamic applications.

To account for the effects of viscoelasticity in the material response, a modified version of the principle of virtual work for irreversible systems can be used, which is

expressed through the following inequality:

$$d\Psi \leq \delta W = F\delta l_1 + v\delta q. \tag{42}$$

The inequality sign in (42) implies that only part of the work done on the RDEA is stored in the material as free-energy, while the rest is dissipated as heat. An in-depth derivation of a visco-elastic model based on (42) has been proposed by several authors (e.g., [36, 40]), and is far beyond the scope of this paper. Here, we only present the final result, and show how to incorporate the viscoelastic effect in the developed RDEA models.

As proven in [36], using the irreversible version of the principle of virtual work (42) as a starting point leads to an additive component $\sigma_{1,irr}$ in the stress σ_1. The additional irreversible component of the stress $\sigma_{1,irr}$ must be chosen in such a way that inequality (42) is satisfied for every system trajectory. Moreover, $\sigma_{1,irr}$ must vanish as the loading frequency tends to zero, so that the reversible version of the model is recovered at steady-state. The equation for the stress hence takes the following general form:

$$\sigma_1 = \sigma_{1,rev} + \sigma_{1,irr}, \tag{43}$$

where the reversible component of the stress $\sigma_{1,rev}$ is given by the expressions for σ_1 in (27), (33), or (39), depending on the considered RDEA model.

An example of model for $\sigma_{1,irr}$ which satisfies the two conditions defined above is provided in the following:

$$\begin{cases} \dot{\xi}_1 = \dfrac{k_{v1}}{\eta_{v1}}\left(\lambda_1 - \xi_1\right) \\ \vdots \\ \dot{\xi}_M = \dfrac{k_{vM}}{\eta_{vM}}\left(\lambda_1 - \xi_M\right) \\ \sigma_{1,irr} = \displaystyle\sum_{j=1}^{M} k_{vj}\left(\lambda_1 - \xi_j\right) + \eta_{v0}\dot{\lambda}_1 \end{cases}. \tag{44}$$

Quantities ξ_j represent internal variables describing the viscoelastic dissipation process, while M, k_{vj}, η_{vj}, and η_{v0} represent constitutive material parameters, with $j \in \{1, \ldots, M\}$. For more details on the proof for which (44) satisfies the required conditions, as well as on the interpretation of model (44), the reader may refer to [36].

4. Experimental Characterization and Validation

The aim of this section is to provide experimental validation of the RDEA model. First, the test-rig used to conduct the experiment is described. Subsequently, an extensive characterization campaign is conducted, with the aim of evaluating the electro-mechanical response of several RDEA specimens with different geometries. The ability of the model to accurately describe the behavior of all the specimens is finally evaluated.

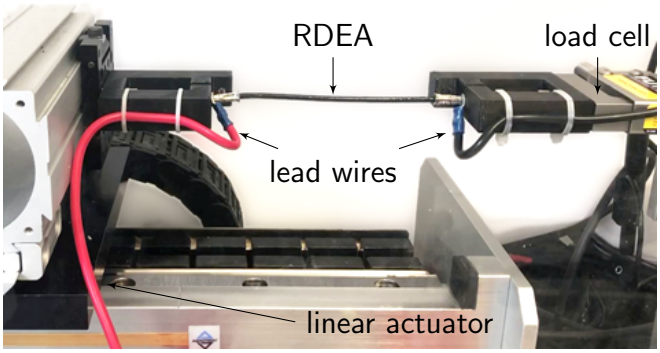

Figure 9: Experimental setup used to characterize the RDEA specimens.

4.1. Experimental Setup

A picture of the experimental setup used to characterize the electro-mechanical response of the RDEA specimens is shown in Figure 9. One end of the RDEA is attached to an Aerotech ACT165DL Linear Actuator, whose displacement can be directly controlled by the user, while its other end is connected to a FUTEK LSB303 Load cell (25 lb) which allows recording the force during deformation. At the same time, a TREK 5/80 High Voltage Amplifier permits to supply an arbitrary high voltage to the RDEA electrodes. Only for the experiments in which no voltage is applied, an additional electrical capacitance measurement is also performed by means of a Rohde & Schwarz HAMEG HM8118 LCR Bridge. Real-time DAQ is implemented via a NI-9149 CompactRIO FPGA chassis with appropriate IO-modules, while data post-processing is performed in LabView and Matlab on a Windows Computer.

The experimental setup described above permits to implement different types of characterization experiments, i.e., force-displacement evaluation with different constant voltage values applied, blocking force tests under cycling voltage input, and capacitance-displacement behavior characterization. All the experiments will be conducted by considering typical ranges of displacement, voltage, and frequency which are relevant for our intended soft robotic application.

4.2. Results and Discussion

For model validation purpose, three silicone-based RDEA samples are designed and manufactured. The corresponding geometric data are reported in Table 1, and consist of a short and thin roll (specimen 1), a short and thick roll (specimen 2), and a long and thin roll (specimen 3). The meaning of the goemetric parameters reported in Table 1 is further clarified in Figure 10. Since our aim is to predict the behavior of all the specimens by means of a unique set of material parameters, the full spectrum of considered geometries provides a challenging validation platform for our model.

Next, we need to choose one of the three models among the ones discussed in Section 3. To this end, we use the procedure outlined in the Appendix to estimate the

Table 1: Physical specimen properties and fixed model parameters.

	Specimen 1	2	3		
L_1	34	34	91	mm	initial length in actuation direction
L_2	58	99	58	mm	initial length in rolling direction (pre-roll)
L_3	48	48	48	µm	single-membrane initial thickness
L_{1e}	29	29	86	mm	length of membrane region with applied electrode along the actuation direction
L_{p1}	10	10	10	mm	electrode-free membrane length at the start of rolling
L_{2e}	38	76	38	mm	length of membrane region with applied electrode along the rolling direction
ϵ_r	2.8				material relative permittivity
ϵ_0	8.85			$\mathrm{pF\,m^{-1}}$	vacuum permittivity

Table 2: Geometric model parameters calculated from unwound membrane dimensions.

	Specimen 1	2	3		
R_i	0.000	0.000	0.000	mm	inner radius of region a
R_{ie}	0.600	0.600	0.600	mm	inner radius of region b
R_{oe}	1.206	1.615	1.206	mm	inner radius of region c
R_o	1.326	1.732	1.326	mm	outer radius of region c

Table 3: Calibrated model parameters (RDEA model).

C_{i0}	242 −69 47	kPa	Yeoh model parameters
M	1		viscoelastic model order
k_{v1}	8271	kPa	viscoelastic model spring stiffness
η_{v1}	86	kPa s	viscoelastic model serial damping
η_{v0}	0	kPa s	viscoelastic model parallel damping

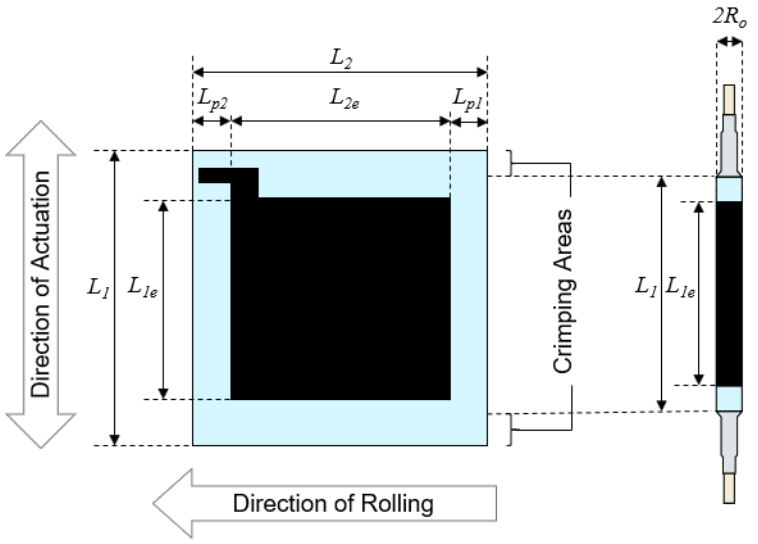

Figure 10: Geometric parameter of the RDEA, before rolling (left-hand side) and after rolling (right-hand side).

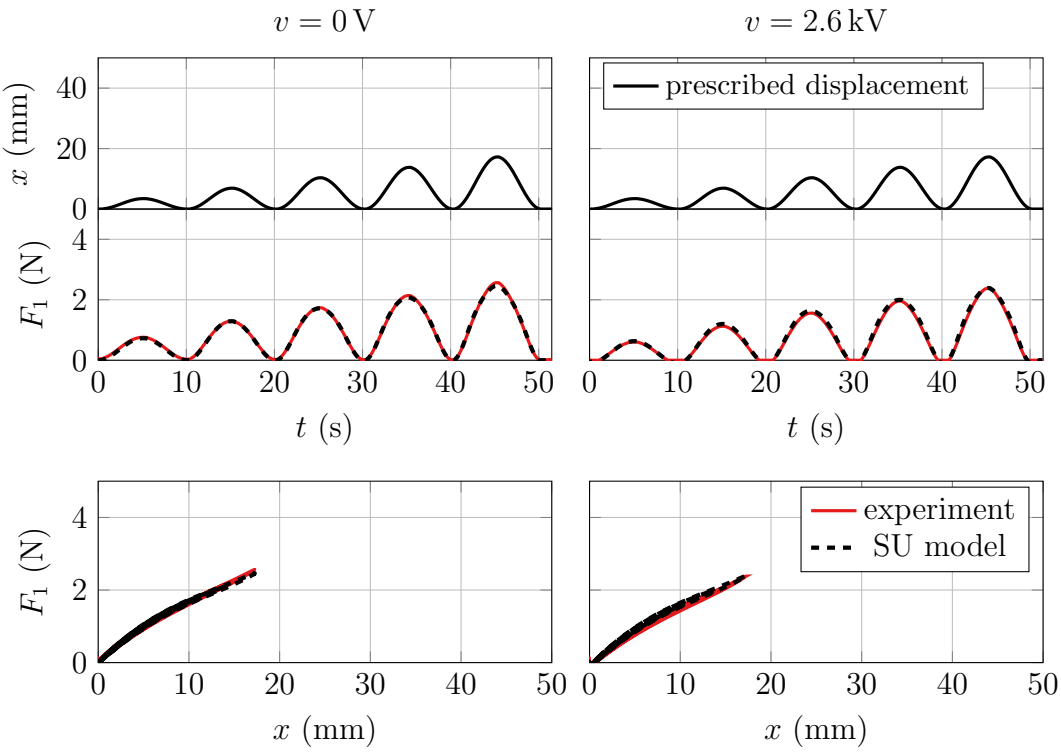

Figure 11: Tensile test for measurements of specimen 1 (solid red line), and model prediction (dashed black line), validation based on SU model. Displacement waveform: sinewave with amplitude modulated by a ramp (solid black line), frequency of 0.1 Hz.

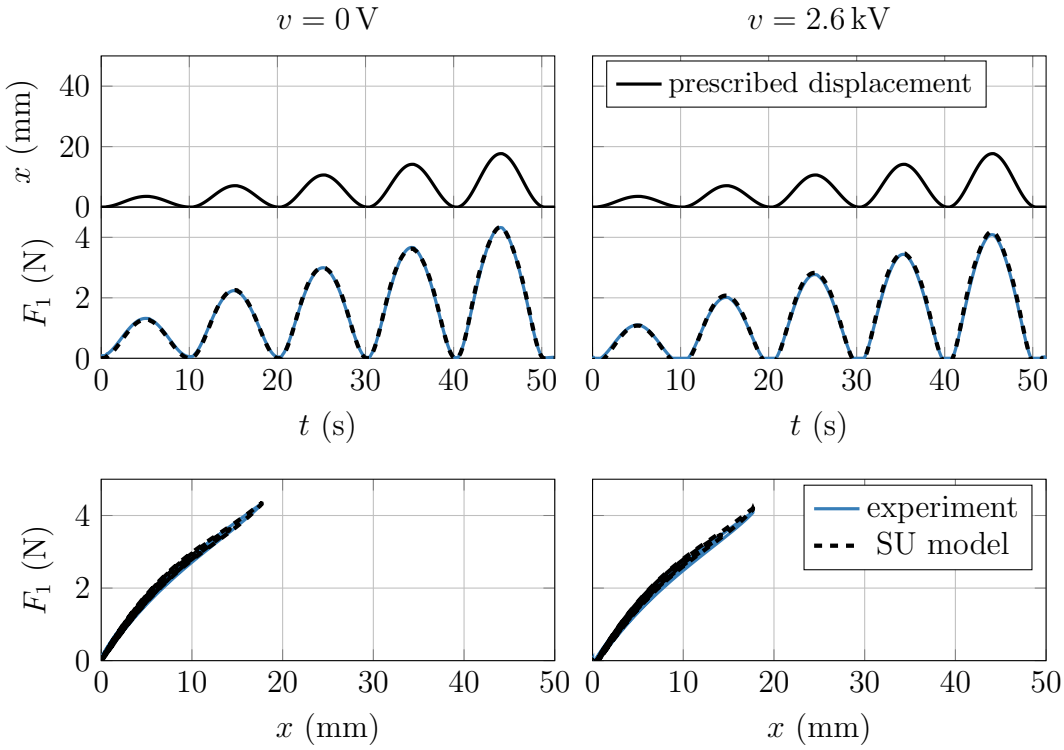

Figure 12: Tensile test for measurements of specimen 2 (solid blue line), and model prediction (dashed black line), calibration based on SU model. Displacement waveform: sinewave with amplitude modulated by a ramp (solid black line), frequency of 0.1 Hz.

rolls radii on the basis of the unwound membrane geometries reported in Table 1. The computed values are reported in Table 2. By inspecting the obtained values for the radii, and recalling the comparative analysis presented in Section 3.4, we conclude that the considered specimens can be consistently and conveniently described by the SU model.

The geometric parameters are all assumed to be measurable, and thus their nominal design values will be used in the following. The material parameters consist of the Yeoh coefficients C_{i0}, $i \in \{1, 2, 3\}$, the permittivity ϵ_r, the viscoelastic model order M and parameters k_{vj}, η_{vj} and η_{v0}, with $j \in \{1, \ldots, M\}$. For the given silicone, the permittivity is assumed to be known and equal to the datasheet value [34], i.e., $\epsilon_r = 2.8$. The remaining Yeoh and viscoelastic parameters, on the other hand, need to be calibrated on the basis of the conducted experiments.

The first set of experiments is performed by deforming the three specimens at different stretch levels up to $\lambda_1 = 1.5$ with a frequency of 0.1 Hz. Each tensile experiment is repeated twice, by considering constant voltage values of $v = 0$ kV and $v = 2.6$ kV. The results of such characterization experiments are reported in Figure 11 for specimen 1 (solid red line), in Figure 12 for specimen 2 (solid blue line), and in Figure 13 for specimen 3 (solid green line). Each plot shows the applied displacement profile and the corresponding membrane force signals over time (upper part), as well as the force-displacement characteristic curve (lower part), for both the $v = 0$ kV (left-hand side)

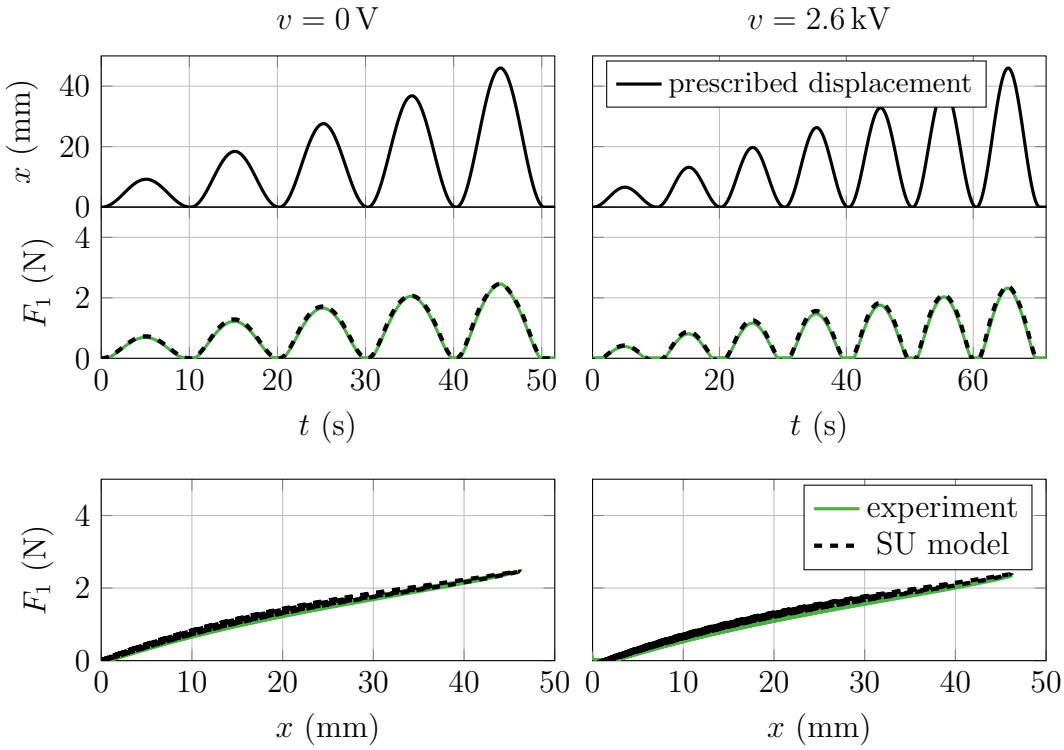

Figure 13: Tensile test for measurements of specimen 3 (solid green line), and model prediction (dashed black line), validation based on SU model. Displacement waveform: sinewave with amplitude modulated by a ramp (solid black line), frequency of 0.1 Hz.

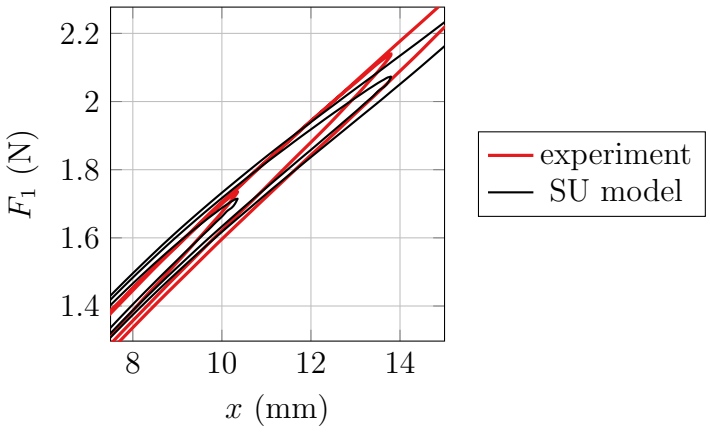

Figure 14: Expanded view based on the force-displacement curve shown in Figure 11 (sample 1, $v = 0$ kV), to highlight the ability of the model in predicting viscoelastic hysteresis. For better visualization, the line style of the model prediction has been modified with respect to Figure 11.

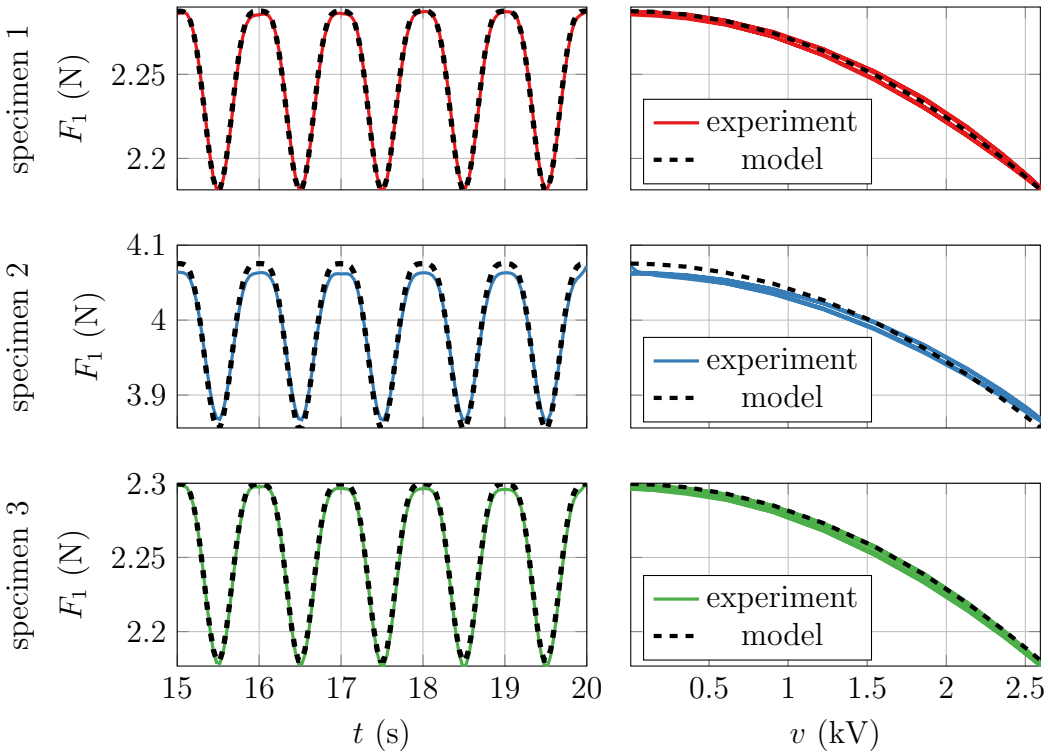

Figure 15: Blocking force comparison, validation based on SU model (left-hand side: force over time, right-hand side: force over voltage). Voltage waveform: sinewave ranging from 0 kV to 2.6 kV, frequency of 1 Hz.

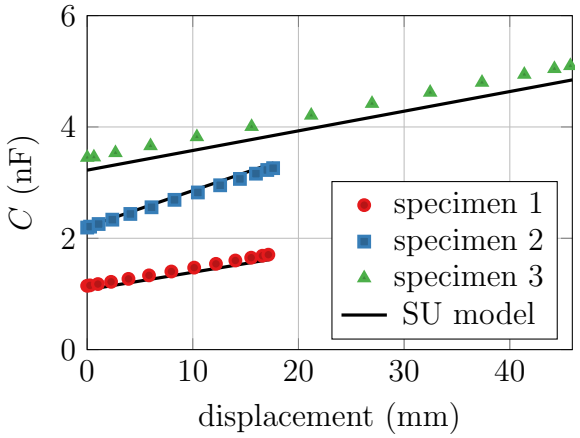

Figure 16: Capacitance comparison, validation based on SU model. Displacement waveform: sinewave with amplitude modulated by a ramp (solid black line), frequency of 0.1 Hz.

Table 4: Numerical accuracy of the model predictions. The maximum relative errors are computed with respect to the maximum experimentally observed force or capacitance, respectively.

Type of experiment	Voltage	Spec.	Max. rel. error (%)
Tensile tests (predicted force) cf. Figures 11 to 13	0 V	1	3.20
		2	5.19
		3	4.81
	2.60 kV	1	6.13
		2	5.41
		3	6.53
Blocking Force cf. Figure 15	0 V to 2.60 kV	1	0.90
		2	0.99
		3	1.18
Capacitance cf. Figure 16	0 V	1	4.99
		2	0.78
		3	5.16

and $v = 2.6$ kV (right-hand side) cases.

All the unknown model parameters are calibrated on the basis of the experimental data for specimen 2 (Figure 12), by means of a nonlinear optimization algorithm based on the Nelder-Mead search method (similarly to [36], details are omitted for conciseness). The resulting set of calibrated parameters is reported in Table 3. These parameters are then used to predict the behavior of the remaining experiments. The resulting model predictions are also shown in Figures 11-13 (dashed black lines). As it can be observed, the model allows reproducing the behavior with remarkable accuracy, for all the geometries and voltage. In addition to that, note how the hysteretic effects due to viscoelasticity are also well reproduced, as highlighted by the expanded view for sample 1 ($v = 0$ kV), reported in Figure 14. For better visualization, the line style of the model prediction in Figure 14 has been modified with respect to Figure 11. Small deviations may be due to manufacturing tolerances, as well as unmodeled local effects, but nevertheless their effect is overall negligible. It is remarked that, due to the linear structure of the viscoelastic stress model (44), we are not able to accurately describe the complex RDEA hysteresis in a wider frequency range. Nevertheless, the adopted model still provides a first order description of the hysteretic trend, which is appropriate for the scope of the present manuscript. Further investigations revealed how the SU model well predicts the RDEAs force-displacement response for higher voltage values as well, up to 4 kV. However, since the material tends to undergo frequent breakdowns if higher voltages are used, further results will be omitted in this paper. A quantitative evaluation of the deviation between experiments and model, expressed in terms of maximum relative

error, is reported in Table 4. As it can be seen, the maximum error is always smaller or equal than 4.81% for $v = 0$ kV, and always smaller or equal than 6.53% for $v = 2.6$ kV, thus confirming the accuracy of our approach. The ability of the SU model in predicting the behavior of specimens with very different geometries confirms the validity of the modeling assumptions outlined in Section 3.

Next, three additional experiments are conducted in which the RDEA position is kept fixed at a stretch of $\lambda_1 = 1.5$, while the voltage is cycled sinusoidally from 0 kV to 2.6 kV at a frequency of 1 Hz, and the resulting blocking force is measured. The resulting data are shown in Figure 15 for all the three specimens (solid red line for specimen 1, solid blue line for specimen 2, solid green line for specimen 3). Based on the parameters calibrated in the previous step, corresponding model predictions are evaluated and plotted in Figure 15 (dashed black lines). Overall, the model is capable of reproducing the behavior of the three geometries with satisfactory accuracy. In particular, relative errors smaller or equal than 1.18% are computed for all those experiments, as reported in Table 4. The highest deviations are observed for specimen 2, but the accuracy still appears satisfactory.

Finally, the ability of the model in predicting the electrical capacitance is investigated. To this end, the capacitance-displacement curves of the three specimens are evaluated based on the same experiments conducted in Figure 11-13, and reported in Figure 16 (solid red line for specimen 1, solid blue line for specimen 2, solid green line for specimen 3). Due to technical limitations of the used LCR meter, the capacitance measurements can be only performed at $v = 0$ kV. The corresponding capacitance values predicted by the model are also reported on the same picture (dashed black lines). The capacitance estimations are solely based on known geometry and permittivity, thus no further parameter calibration is performed when generating the simulation results in Figure 16. A remarkable agreement is observed also in this case, both in terms of the initial capacitance and the resulting trend. Small deviations, visible especially for specimen 3, could be due to manufacturing inaccuracies as well as parasitic effects. The latter assumption is supported by the fact that the experimental curve for specimen 3 has the same slope than the simulated one, but is characterized by a higher offset, which could be well explained by an added constant parasitic capacitance. Nevertheless, the overall accuracy is high, with errors always smaller or equal than 5.16% for all the specimens, as reported in in Table 4. The linear dependency between capacitance and displacement, which is both predicted theoretically (cf. (41)) and confirmed experimentally, suggests the possibility of effectively implementing self-sensing schemes in the future, which will allow developing a sensorless control architecture for RDEAs.

Based on the results reported in Figures 11-16, it can be concluded that the proposed SU model represents the optimal choice when dealing with the considered class of core-free RDEAs, as it accurately captures the experimental results while requiring minimum computational cost.

5. Conclusion

In this work, we presented a lumped-parameter modeling approach for thin, core-free, rolled dielectric elastomer actuators (RDEAs). Starting from a free-energy approach, we derived a physics-based general model which estimates the RDEA force and capacitance by knowing its elongation and voltage, and accounts for several effects such as hyperelasticity, electro-mechanical coupling, viscoelasticity, and geometry scaling. The proposed general model takes into account inhomogeneities in the radial stretch and electric field distributions over different regions of the actuator, due to the simultaneous presence of electrically active and shielding passive layers. Based on the general model, reduced-order and computationally efficient models are proposed, which are suitable to describe RDEAs with different geometric features.

Experimental validation, conducted on three custom-developed RDEA specimens having different geometries (a short and thin one, a short and thick one, and a long and thin one), showed how the proposed modeling approach permits to predict all the measured data with great accuracy. Not only is the model able to reproduce the RDEA response in tensile experiments (force-displacement characterization for different constant voltage values), blocking force tests (force-voltage characterization for different constant displacement values), and capacitance characterization investigations, but it also foresees the effect of the geometry scaling on the overall electro-mechanical response with remarkable accuracy. Based on the obtained results, it can be concluded that the model represents an accurate and numerically efficient tool for simulation, design optimization, and real-time control/self-sensing applications. Moreover, we point out that the model is built upon a strongly uniaxial assumption, i.e., circumferential and radial stretches are always equal regardless of the applied electro-mechanical load. This differs from what is commonly observed in unwound strip-shaped DE membranes made of the same material, in which uniaxiality solely holds when a purely mechanical load (with no electric field) is applied. The results of the experimental validation seem to confirm this interesting, yet not intuitive at a first glance, result for core-free DEAs.

In future research, the developed model will be coupled with models of flexible structures, and used to simulate and optimize RDEA-driven soft robotic systems. A special focus will be put on how to pre-stretch the RDEAs in an optimal way, by combining the results previously published in [35] with the improved transducer model presented in this work. In addition, we will investigate more extensively the dynamic response of the RDEAs when subjected to the complex loading conditions, such as the ones occurring in soft robotic structures. The resulting coupled models will then be used to develop advanced motion control and self-sensing strategies for DE-based soft robots.

Acknowledgments

The authors gratefully acknowledge the support of the Deutsche Forschungsgemeinschaft (DFG, German Research Foundation) through Priority Program SPP 2100 "Soft Material Robotic Systems" (Projects: SE704/6-1,RI3030/1-1). GM received funds from European Union's Horizon 2020 research and innovation programme under the Marie Sklodowska-Curie grant agreement No 893674 (DEtune).

Appendix. Calculation of the Hollow Cylinders Radii from the Unwound DE Membrane Dimensions

In order to accurately compare the RDEA model to the experiments, it is crucial to carefully calculate the model parameters based on the available measured dimensions and other known properties of the physical specimens. On the one hand, measuring the dimensions of the flat DE membranes prior to rolling is relatively simple. On the other hand, the model requires the knowledge of the radii of the different cylindrical regions, which might be hard, if not impossible, to measure exactly after the rolling process has been performed. This section provides a systematic procedure to estimate the radii of the RDEA, starting from the geometry of the unwound DE membrane. The key idea is based on accurately matching the volumes of active and inactive regions before and after the rolling.

As explained in Section 2, the RDEA is manufactured by rolling a stack of two planar membranes with known dimensions. Figure 17 illustrates the resulting structure of a RDEA cross-section from a modeling perspective. The meaning of each parameter is reported in Table 1, and further visualized in Figure 10. Starting from the center and moving outwards radially, the spiral describing the wound DE membranes starts at a given inner radius R_i, and completes a certain amount of turns (described by the accumulated turning angle θ_{p1}) until the entire length L_{p1} of the inner electrode-free membrane is covered. Once this point is reached, the electrode-covered portion of the membrane stack begins. If a voltage is applied to the electrodes, an electric field will be induced in the region between them, as denoted by the arrows in Figure 17a. Note that, in the first turn with electrodes, the electric field only appears in the outer half of the membrane stack, while in subsequent turns it also manifests itself in the inner half. This is due to the fact that the negative electrode of the current turn forms an additional pair with the positive electrode of the previous turn. This geometric feature produces a corresponding loss of active electrical volume, which is considered in the following calculations. In addition, the second passive layer of length L_{p2} produces a further electric field-free region on the outermost part of the roll, corresponding to angle θ_{p2} in Figure 17a. Note how this figure does not depict the passive layers in a realistic way (cf. Figure 3a), but solely serves to provide a geometric intuition for angles θ_{p1} and θ_{p2}.

A suitable kinematic model for describing the spiral geometry is the Archimedean

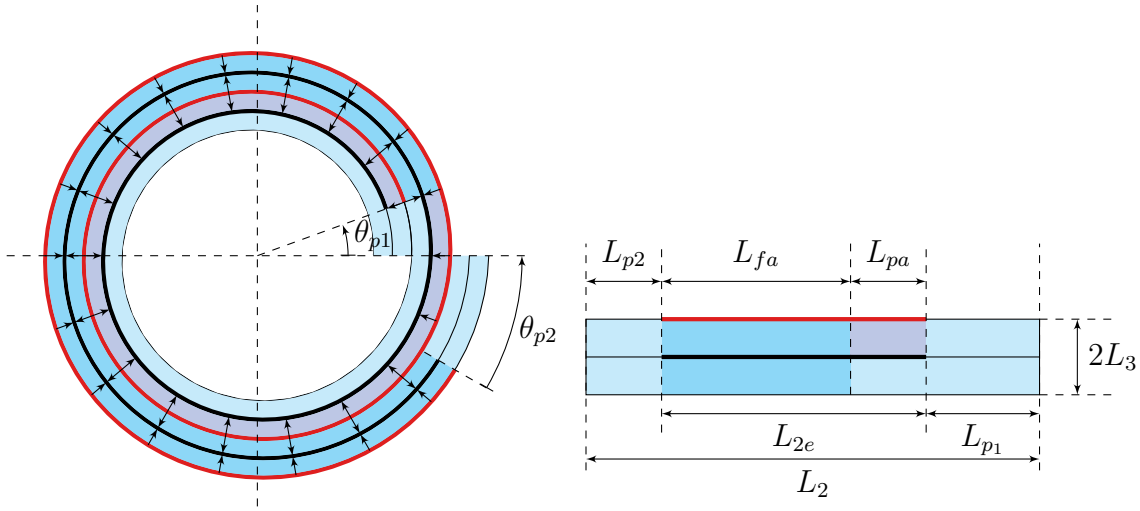

(a) Cross-Sectional view. (b) Virtually unrolled view.

Figure 17: Passive, partially active, and fully active regions of a RDEA.

spiral, which is characterized by having a constant separation between adjacent turns. The Archimedean spiral can be expressed in polar coordinates as

$$r(\theta) = r_0 + \frac{d}{2\pi}\theta \qquad \text{with} \quad r_0, d \in \mathbb{R}^+, \tag{45}$$

where the spiral radius r is given as a function of the turning angle θ, r_0 indicates the starting radius of the spiral, and d is the separation between adjacent turns. The circumference, or length, of such a spiral is obtained by solving the following integral:

$$l_{\text{spiral}}(r_0, d, \theta) = \int_0^{\theta} \left\| \frac{d}{d\bar{\theta}} \left(r(\bar{\theta}) \begin{bmatrix} \cos\bar{\theta} \\ \sin\bar{\theta} \end{bmatrix} \right) \right\|^2 d\bar{\theta}. \tag{46}$$

Although an analytical solution is available for (46), in here it is omitted for conciseness. The total turning angle as a function of the spiral length is thus given as the inverse function of l_{spiral}:

$$\theta_{\text{spiral}}(r_0, d, l_{\text{spiral}}) = l^{-1}_{\text{spiral}}(r_0, d, l_{\text{spiral}}). \tag{47}$$

In practice, (47) is generally solved with numerical methods.

Based on equations (46)-(47), it is now possible to compute the geometric parameters appearing in Figure 17b which are related to the losses in active volume caused by the passive regions (green areas in Figure 17a). The turning angle θ_{p1} denotes the start of the electrically half-active region, consisting of the first turn with electrodes (purple area in Figure 17a), and is computed as follows:

$$\theta_{p1} = \theta_{\text{spiral}}(R_i, 2L_3, L_{p1}). \tag{48}$$

To obtain (48), the following substitutions are made in (47): $r_0 = R_i$, $d = 2L_3$, and $l_{\text{spiral}} = L_{p1}$ (c.f. Table 1). The electrically half-active region starts at θ_{p1} and ends after

one full turn, which means at turning angle $\theta_{p1} + 2\pi$. We can thus calculate the length L_{pa} of the partially active region as:

$$L_{pa} = l_{spiral}(R_i, 2L_3, \theta_{p1} + 2\pi) - L_{p1}. \tag{49}$$

The remaining length L_{fa} of the fully active region (cyan area in Figure 17a) is given as the difference between total electrode length and partially active length:

$$L_{fa} = L_{2e} - L_{pa}. \tag{50}$$

Finally, the length of the outer inactive region is given by:

$$L_{p2} = L_2 - L_{p1} - L_{2e}. \tag{51}$$

The above computed quantities can readily be used to compute the equivalent radii of the hollow cylinders describing the RDEA. When discussing the RDEAs basics in Section 2, it is remarked how the adopted manufacturing process allows obtaining rolls in which the hollow central region is very small. This is also confirmed by the microscope picture in Figure 3a, in which no meaningful inner hollow region can be seen. Based on this argument, we set

$$R_i = 0. \tag{52}$$

The three remaining radii are then computed by equating the volumes of the three hollow cylinders with the ones of the corresponding regions in the flat membrane state, according to Figure 17:

$$\Omega_a = \pi(R_{ie}^2 - R_i^2)L_1 = L_1 L_3(2L_{p1} + L_{pa}), \tag{53}$$
$$\Omega_b = \pi(R_{oe}^2 - R_{ie}^2)L_1 = L_1 L_3(2L_{fa} + L_{pa}), \tag{54}$$
$$\Omega_c = \pi(R_o^2 - R_{oe}^2)L_1 = 2L_1 L_3 L_{p2}. \tag{55}$$

Note that the partially active volume is distributed equally between regions a and b. Solving (55) for the unknown radii, by considering positive solutions only, the following expressions are obtained:

$$R_{ie} = \sqrt{\frac{2L_3 L_{p1} + L_3 L_{pa}}{\pi}}, \tag{56}$$
$$R_{oe} = \sqrt{\frac{2L_3 L_{fa} + L_3 L_{pa}}{\pi} + R_{ie}^2}, \tag{57}$$
$$R_o = \sqrt{\frac{2L_3 L_{p2}}{\pi} + R_{oe}^2}. \tag{58}$$

References

[1] Carpi F, Rossi D D, Kornbluh R, Pelrine R E and Sommer-Larsen P 2011 *Dielectric Elastomers as Electromechanical Transducers: Fundamentals, Materials, Devices, Models and Applications of an Emerging Electroactive Polymer Technology* (Elsevier) ISBN 978-0-08-055772-4

[2] Gu G Y, Zhu J, Zhu L M and Zhu X 2017 *Bioinspiration & biomimetics* **12** 011003
[3] Gupta U, Qin L, Wang Y, Godaba H and Zhu J 2019 *Smart Materials and Structures* **28** 103002
[4] Huang B, Li M, Mei T, McCoul D, Qin S, Zhao Z and Zhao J 2017 *Sensors* **17** 2708
[5] Zhao H, Hussain A M, Israr A, Vogt D M, Duduta M, Clarke D R and Wood R J 2020 *Soft robotics* **7** 451–461
[6] Kovacs G, Düring L, Michel S and Terrasi G 2009 *Sensors and actuators A: Physical* **155** 299–307
[7] Hau S, Bruch D, Rizzello G, Motzki P and Seelecke S 2018 *Smart Materials and Structures* **27** 074003
[8] Berselli G, Vertechy R, Vassura G and Parenti-Castelli V 2011 **16** 13
[9] Plante J and Dubowsky S 2007 *Smart Materials and Structures* **16** S227
[10] Kofod G, Wirges W, Paajanen M and Bauer S 2007 *Applied Physics Letters* **90** 081916
[11] Li T, Keplinger C, Baumgartner R, Bauer S, Yang W and Suo Z 2013 *Journal of the Mechanics and Physics of Solids* **61** 611–628
[12] White P, Latscha S and Yim M 2014 Modeling of a dielectric elastomer bender actuator *Actuators* vol 3 (Multidisciplinary Digital Publishing Institute) pp 245–269
[13] Kornbluh R D, Pelrine R, Pei Q, Heydt R, Stanford S, Oh S and Eckerle J 2002 Electroelastomers: applications of dielectric elastomer transducers for actuation, generation, and smart structures *Smart Structures and Materials 2002: Industrial and Commercial Applications of Smart Structures Technologies* vol 4698 (International Society for Optics and Photonics) pp 254–270
[14] Kunze J, Prechtl J, Bruch D, Fasolt B, Nalbach S, Motzki P, Seelecke S and Rizzello G 2021 **10** 69
[15] Benslimane M Y, Kiil H E and Tryson M J 2010 *Polymer International* **59** 415–421
[16] Lau G K, Lim H T, Teo J Y and Chin Y W 2014 *Smart Materials and Structures* **23** 025021
[17] Zhang R, Lochmatter P, Kunz A and Kovacs G M 2006 Spring roll dielectric elastomer actuators for a portable force feedback glove *Smart Structures and Materials 2006: Electroactive Polymer Actuators and Devices (EAPAD)* vol 6168 (International Society for Optics and Photonics) p 61681T
[18] Rajamani A, Grissom M D, Rahn C D and Zhang Q 2008 *IEEE/ASME Transactions on Mechatronics* **13** 117–124 ISSN 1083-4435 URL http://ieeexplore.ieee.org/document/4453931/
[19] Pei Q, Pelrine R, Stanford S, Kornbluh R and Rosenthal M 2003 *Synthetic Metals* **135** 129–131
[20] Ren K, Liu S, Lin M, Wang Y and Zhang Q 2008 *Sensors and Actuators A: Physical* **143** 335–342
[21] Levard T, Diglio P J, Lu S G, Rahn C D and Zhang Q 2011 *Smart materials and structures* **21** 012001
[22] Kunze J, Prechtl J, Bruch D, Nalbach S, Motzki P, Seelecke S and Rizzello G 2020 Design and fabrication of silicone-based dielectric elastomer rolled actuators for soft robotic applications *Electroactive Polymer Actuators and Devices (EAPAD) XXII* vol 11375 (International Society for Optics and Photonics) p 113752D
[23] Kovacs G M, Ha S M, Michel S, Pelrine R and Pei Q 2008 Study on core free rolled actuator based on soft dielectric eap *Electroactive Polymer Actuators and Devices (EAPAD) 2008* vol 6927 (International Society for Optics and Photonics) p 69270X
[24] Chen Y, Zhao H, Mao J, Chirarattananon P, Helbling E F, Hyun N s P, Clarke D R and Wood R J 2019 *Nature* **575** 324–329 ISSN 1476-4687 number: 7782 Publisher: Nature Publishing Group URL https://www.nature.com/articles/s41586-019-1737-7
[25] Zhao H, Hussain A M, Duduta M, Vogt D M, Wood R J and Clarke D R 2018 *Advanced Functional Materials* **28** 1804328
[26] Pei Q, Rosenthal M, Stanford S, Prahlad H and Pelrine R 2004 *Smart materials and structures* **13** N86
[27] Coyle S, Majidi C, LeDuc P and Hsia K J 2018 *Extreme Mechanics Letters* 9
[28] Youn J H, Jeong S M, Hwang G, Kim H, Hyeon K, Park J and Kyung K U 2020 *Applied Sciences* **10** 640

[29] Wissler M and Mazza E 2007 *Sensors and Actuators A: Physical* **138** 384–393
[30] Li J, Liu L, Liu Y and Leng J 2019 *Soft robotics* **6** 69–81
[31] Carpi F and De Rossi D 2004 *Materials Science and Engineering: C* **24** 555–562 ISSN 09284931 URL https://linkinghub.elsevier.com/retrieve/pii/S0928493104000384
[32] Jones R W and Sarban R 2012 *Smart Materials and Structures* **21** 075019
[33] Prechtl J, Kunze J, Bruch D, Seelecke S and Rizzello G 2021 Modeling and parameter identification of rolled dielectric elastomer actuators for soft robots *Electroactive Polymer Actuators and Devices (EAPAD) XXIII* vol 11587 (International Society for Optics and Photonics) p 115871H
[34] Elastosil 2030 films catalogue, Wacker https://www.wacker.com/h/medias/7091-EN.pdf
[35] Prechtl J, Kunze J, Bruch D, Seelecke S and Rizzello G 2021 Bistable actuation in multi-dof soft robotic modules driven by rolled dielectric elastomer actuators *IEEE International Conference on Soft Robotics RoboSoft2021* vol 11587 (IEEE) pp 1–8
[36] Rizzello G, Loew P, Agostini L, Fontana M and Seelecke S 2020 *Smart Materials and Structures* **29** 115030
[37] Wissler M and Mazza E 2005 *Sensors and Actuators A: Physical* **120** 184–192 ISSN 0924-4247 URL http://www.sciencedirect.com/science/article/pii/S0924424704008258
[38] Suo Z 2010 *Acta Mechanica Solida Sinica* **23** 549–578
[39] He T, Zhao X and Suo Z 2009 *Journal of Applied Physics* **106** 083522
[40] Chiang Foo C, Cai S, Jin Adrian Koh S, Bauer S and Suo Z 2012 *Journal of Applied Physics* **111** 034102